

Probing reionization using quasar near-zones at redshift $z \sim 6$

Hamsa Padmanabhan^{1*}, T. Roy Choudhury^{2†}, R. Srianand^{1‡}

¹ *Inter-University Centre for Astronomy and Astrophysics, Pune 411007, India*

² *National Centre for Radio Astrophysics, Tata Institute of Fundamental Research, Pune 411007, India*

ABSTRACT

Using hydrodynamical simulations coupled to a radiative transfer code, we study the additional heating effects in the intergalactic medium (IGM) produced by $z \sim 6$ quasars in their near-zones. If helium is predominantly in He II to begin with, both normalization (T_0) and slope (γ) of the IGM effective equation-of-state get modified by the excess ionization from the quasars. Using the available constraints on T_0 at $z \sim 6$, we discuss implications for the nature and epoch of H I and He II reionization. We study the extent of the He III region as a function of quasar age and show, for a typical inferred age of $z \sim 6$ quasars (i.e. $\sim 10^8$ yrs), it extends up to 80% of the H I proximity region. For these long lifetimes, the heating effects can be detected even when all the H I lines from the proximity region are used. Using the flux and curvature probability distribution functions (PDFs), we study the statistical detectability of heating effects as a function of initial physical conditions in the IGM. For the present sample size, cosmic variance dominates the flux PDF. The curvature statistics is more suited to capturing the heating effects beyond the cosmic variance, even if the sample size is half of what is presently available.

Key words: dark ages, reionization, first stars - intergalactic medium - quasars : absorption lines

1 INTRODUCTION

Unravelling the process of reionization, which signals the end of the ‘dark ages’ of our universe, is one of the current challenges of observational and theoretical cosmology. Two major milestones in the reionization history of the universe are those of hydrogen (H I) and singly ionized helium (He II). Study of the evolution of hydrogen reionization combines observational evidences from various sources; optical probes include the Gunn-Peterson absorption troughs (Gunn & Peterson 1965) in the spectra of high-redshift bright sources such as (a) quasars (Fan, Carilli & Keating 2006; Willott et al. 2007; Mortlock et al. 2011), (b) Lyman- α emitters (Kashikawa et al. 2006; Stark et al. 2007; Ouchi et al. 2010; Nakamura et al. 2011) and (c) γ -ray bursts (GRBs; Totani et al. 2006; Kistler et al. 2009; Ishida, de Souza & Ferrara 2011; Robertson & Ellis 2012). The Thomson scattering optical depth measurements from the Cosmic Microwave Background (CMB) temperature and polarization power spectra are consistent with an instantaneous reionization at redshift $z \sim 11$ (Larson et al. 2011; Planck Collaboration et al. 2013; Komatsu et al. 2011), which may be interpreted as an estimate of the mean reionization redshift. At radio frequencies, the redshifted 21-cm hyperfine line of neutral hydrogen promises a unique three-dimensional

mapping of the epoch of reionization (EoR) of hydrogen (for a review, see Furlanetto, Oh & Briggs 2006). All the available observations at present are consistent with an extended H I reionization history that probably began at $z \sim 15$ and ended around $z \sim 6$ (Wyithe & Loeb 2003; Choudhury & Ferrara 2005, 2006; Pritchard & Loeb 2010; Pritchard, Loeb & Wyithe 2010; Mitra, Choudhury & Ferrara 2011, 2012).

The current observational probes of He II reionization include measuring the Gunn-Peterson absorption troughs in the He II Lyman- α forest (Jakobsen et al. 1994; Zheng et al. 2004; Reimers et al. 2005; Shull et al. 2010; Worseck et al. 2011; Syphers & Shull 2014). These observations suggest that the EoR of He II is close to $z \sim 2.7$. The reionization of He II also leaves a thermal imprint on the hydrogen Lyman- α forest due to the additional heating effect on the velocity widths of the Lyman- α lines (Hui & Gnedin 1997). The thermal evolution of the intergalactic medium (IGM) from $2 \leq z \leq 4.8$ has been probed using the observations of the Lyman- α forest (Ricotti, Gnedin & Shull 2000; Schaye et al. 2000; McDonald et al. 2001). The velocity widths of the hydrogen Lyman- α forest lines seem to exhibit a sudden increase between redshifts $z \sim 3.5$ and 3, which may represent evidence for the reionization of He II. The inferred temperature measurements, taken in conjunction with the adiabatic cooling expected to occur after the reionization of hydrogen, also constrain the EoR of hydrogen to below $z \sim 9$ (Theuns et al. 2002). Recently, Becker et al. (2011) reported measurements of the IGM temperature from $2 \leq z \leq 4.8$ using the curvature statistic to

* Electronic address: hamsa@iucaa.ernet.in

† Electronic address: tirth@ncra.tifr.res.in

‡ Electronic address: anand@iucaa.ernet.in

quantify the temperature; their observations indicated gradual heating of the IGM from $z \sim 4.4$ towards lower redshifts, in contrast to the adiabatic cooling expected in single-step models of reionization. These measurements are consistent with an extended epoch of He II reionization starting probably at $z \gtrsim 4.4$ and terminating around $z \sim 3$.

Helium is expected to be singly ionized around the same time as the hydrogen gets ionized, and first-generation galaxies are believed to be the likely sources for completion of hydrogen and He I reionization. In the single-step model of reionization, it is believed that massive, metal-free Population III stars (Oh et al. 2001; Venkatesan, Tumlinson & Shull 2003) may have provided the hard photons required for He II reionization. In this model, a population of metal-free (Pop III) stars are required at redshifts $z > 6$ to reionize both H I and He II. In the absence of a strong ionizing background for He II, it may recombine and hence to be reionized again at a lower redshift. Therefore, probes of intergalactic He II are important for understanding the role of Population III stars in the early reionization of He II and setting up a He II ionizing background prior to the quasar era (i.e. $z \sim 6$). Recently, there are indications of the presence of Population III stars even as late as $z \sim 3$ possibly due to inefficient transport of heavy elements and/or poor mixing that leave pockets of pristine gas even in chemically evolved galaxies (Jimenez & Haiman 2006; Tornatore, Ferrara & Schneider 2007; Inoue et al. 2011; Cassata et al. 2013). If, on the other hand, reionization took place as a two-step process (hydrogen first and He II later), quasars¹ are believed to be the most likely candidates for reionization of He II since their spectra are sufficiently hard. However, the number density of bright quasars peaks at $z \sim 2 - 3$ and decreases rapidly above $z \sim 4$ (Assef et al. 2011; Masters et al. 2012). Hence, in the two-step model of reionization, the final stages of He II reionization are expected to coincide with the peak of the quasar activity at $z \sim 2 - 3$.

Quasar proximity zones², where the excess ionization by the quasar allows the measurement of the velocity width of the Lyman- α line, have been used to probe the thermal state of the IGM at $z \sim 6$ (Bolton et al. 2010). This, in turn, can be used to probe the role of quasars in He II reionization. The IGM temperature in the near-zone³ is influenced by both the existing background radiation as well as the additional radiation from the quasar itself. A first measurement of the near-zone temperature around a quasar at redshift 6 has been reported in Bolton et al. (2010) using Keck/HIRES data in combination with hydrodynamical simulations. Recently, an additional source of heating has been observed in the ionized near-zones of high-redshift quasars at $z \sim 6$, which is attributed (Bolton et al. 2012) to the initial stages of helium reionization around that redshift, since the excess heating can be easily accounted for if the He II is ionized by the quasar. The inferred excess temperature in the quasar near-zone can be used to

place constraints on the epoch of H I reionization (see, for example, Ciardi et al. 2012; Raskutti et al. 2012).

In this paper, we explore several aspects of the additional heating effect in the near-zones of quasars at $z \sim 6$ using the results of high-resolution hydrodynamical (SPH) simulations with GADGET-2 (Springel 2005), and the ionization correction done using a 1D radiative transfer code which we have developed. The gas temperature in the general IGM is given by the assumed equation of state (Hui & Gnedin 1997) and computed self-consistently for the near-zone of the quasar. We first validate our simulations by computing the additional temperature in the near zone for different initial equations of state of the general IGM, and different assumed values of the He II fraction prior to the active quasar phase. We obtain the expected relationship between the excess temperature and the initial He II fraction in the quasar near-zone, and also find a connection between the magnitude of the steepening of the equation of state and the initial He II fraction. We then use our simulation results to measure the size of the region in the near-zone heated by the quasar in comparison to the H I proximity zone, as a function of the age of the quasar. We also validate the usage of the flux and curvature statistics to measure the increased temperature in the near-zone of the quasar, and, in particular, address the effect of cosmic variance. For the flux statistics tests, we employ a number of pixels typical of the sample sizes in available observations of quasar near-zones at redshifts ~ 6 . Using the Kolmogorov-Smirnov (KS) statistic to quantify the effect of the additional heating, and examining its variation with the parameters of the equation of state, T_0 and γ , we establish the connection between the thermal evolution of the IGM following the reionization of hydrogen, and the detectability of the additional heating in the quasar near-zone. We also consider the possible dependence of the detectability of the additional heating effect on the assumed values of the background (metagalactic) photoionization rate of He II, which translates into varying the He II fraction in the near-zone of the quasar. This allows a connection to the effect of Population III stars on reionizing He II at redshifts $z > 6$ (which constrains the initial He II fraction in the quasar near-zone) in single-step reionization scenarios.

The paper is organized as follows: In Sec. 2, we describe our hydrodynamical simulations and the numerical formalism for obtaining the simulated spectra in the quasar near-zone. In Sec. 3, we provide a validation of our simulations by computing the excess temperature in the quasar near-zone for different values of the equation of state normalization, and the initial He II fraction, with comparison to the measured average temperature (Bolton et al. 2012) in seven quasar near-zones at redshift ~ 6 . We also describe the modification to the initial equation of state of the IGM due to the additional heating, and its dependence on the initial He II fraction in the quasar near-zone. In Sec. 4, we describe the results obtained from our calculations as regards (a) the extent of the region around the quasar within which the additional heating is expected to contribute significantly, (b) the dependence of the additional heating effect in the near-zone on the initial equation of state of the IGM, quantified by the flux and curvature statistics, and (c) the dependence of the heating effect on the initial He II fraction in the near-zone, which is related to the single-step reionization by Population III stars. We then summarize our findings in a brief concluding section. Throughout this article, we assume the cosmological parameters $\Omega_m = 0.26$, $\Omega_\Lambda = 0.74$, $\Omega_b h^2 = 0.024$, $h = 0.72$, $\sigma_8 = 0.85$, and $n_s = 0.95$, which are consistent with the third-year WMAP and Lyman- α forest data (Seljak, Slosar & McDonald 2006; Viel, Haehnelt & Lewis 2006). The helium fraction by mass is taken to be 0.24 (Olive & Skillman 2004).

¹ Strictly speaking, the term ‘quasar’ is reserved for describing radio-loud quasi-stellar objects. However, as frequently done in the literature, we will use the term ‘quasars’ in this paper to indicate quasi-stellar objects, irrespective of their radio properties.

² Here, and in what follows, the term “proximity zone” or “H I proximity zone” describes the region in the vicinity of the quasar where the ionizing flux from the quasar dominates the background flux.

³ Here, and in what follows, the term “near zone” refers to the region in the vicinity of the quasar within the He III ionization front, where the heating effects are significant.

2 BRIEF DESCRIPTION OF NUMERICAL STUDY

2.1 Hydrodynamical simulations and simulated spectra

We perform cosmological hydrodynamical simulations using the parallel smoothed-particle hydrodynamics (SPH) code GADGET-2 (Springel 2005). We use two sets of simulations in this work: the lower resolution simulation contains 256^3 each of gas and dark matter particles in a periodic box of size $60h^{-1}$ comoving Mpc, and the high resolution simulation contains 512^3 each of gas and dark matter particles in a periodic box of size $10h^{-1}$ comoving Mpc. In both cases, the gravitational softening length is 1/30th of the mean interparticle spacing, and initial conditions are generated following the transfer function of Eisenstein and Hu (Eisenstein & Hu 1999). Both sets of simulations are started at $z = 99$. Output baryonic density and velocity fields are generated at redshift $z \sim 6$.

Recently, it has been shown that when AGN feedback effects are taken into account in simulations, one finds that quasar host galaxies at redshifts ~ 6 are not ‘special’ (Fanidakis et al. 2013). It is now recognized that the existence of overdensities in the quasar near-zone can influence the background H I photoionization rate measurements using the proximity effect (Rollinde et al. 2005; Guimarães et al. 2007; Faucher-Giguère et al. 2008), but the thermal effects of choosing the quasar in a random position as compared to locating them in a high density environment may be minor (Raskutti et al. 2012, see Section 4.3 of the paper). Observationally, Willott et al. (2005) find no evidence of an overdensity of i-dropout galaxies around three $z \sim 6$ quasars, Kim et al. (2009) find only two out of five quasar fields showing any evidence of overdensity, and Bañados et al. (2013), studying the environment of a redshift 5.72 quasar, find no enhancement of Lyman- α emitters in the surroundings, compared to the blank fields. For most part of this work, we make the implicit assumption that quasars are not “special” and hence do not arise preferentially in biased regions. However, we come back to this point and provide a qualitative discussion of the effects of locating the quasars in biased regions, in Sec. 4.4.

Lines of sight are extracted randomly in each simulation box at redshift 6, and the density and velocity fields along each line-of-sight is obtained. From the density grid of baryons in the simulation box, we compute the (physical) number densities of hydrogen and helium, n_{H} and n_{He} (assuming the mass fraction $Y = 0.24$ of helium) and then solve the equilibrium photoionization equations for H I, He I and He II. Here, we explicitly assume that the universe is already reionized and the IGM, assumed to be optically thin, is in photoionization equilibrium with the background. The background ionizing radiation is assumed to follow the optically thin photoionization rates of hydrogen and helium as predicted by the “quasars + galaxies” Haardt-Madau background at redshift ~ 6 , i.e. Table 3 of Haardt & Madau (2012). The value of the background H I photoionization rate considered here is consistent at the 1σ level with the results of the simulations of Bolton & Haehnelt (2007b) and the observations of quasar proximity zone sizes in Wyithe & Bolton (2011). It is slightly higher than the value $(1.57 \pm 0.62) \times 10^{-13} \text{ s}^{-1}$, measured by Calverley et al. (2011) using quasar proximity effects. The background He II photoionization rate, $\Gamma_{\text{HeII}}^{\text{bg}}$, is known to have large fluctuations even at $z \sim 3$ due to the small number of ionizing sources within the characteristic mean free path of ionizing photons (see, for example, Fardal, Giroux & Shull 1998; Furlanetto 2009; Khaire & Srikanth 2013). At $z \sim 6$, this effect is expected to be severe, and the $\Gamma_{\text{HeII}}^{\text{bg}}$ we use is very small and should be treated as representative only. Later, we study the effect of varying this parameter on the results obtained.

In the absence of additional radiation from the quasars, we as-

sign the gas temperature to each pixel by using the equation of state of the photoionized IGM (Hui & Gnedin 1997) with the normalization temperature $T_0 = 10^4$ K, and the slope $\gamma = 1.3$. In principle, T_0 and γ at a given epoch can be fixed by comparing model predictions with observations. Later, we also explore some models with physically motivated ranges in T_0 and γ and draw conclusions regarding the epoch of H I reionization.

We now evolve of temperatures and ion densities of hydrogen and helium (caused by ionization due to the quasar as well as the metagalactic background) along a line of sight with the quasar placed at the first gridpoint. The four parameters, the temperature (obtained by using the equation of state) and the ion densities of H I, He II and He III (obtained under the equilibrium conditions with the photoionization rates from the background, i.e. without contribution from the quasar) are incorporated as initial conditions. The luminosity of the quasar at the Lyman edge, L_{HI} , is computed from the magnitude $M_{\text{AB}} = -26.67$ at 1450 \AA (a typical magnitude for a luminous quasar at redshift ~ 6). We assume the broken power law spectral index of $f_\nu \propto \nu^{-0.5}$, $1050 \text{ \AA} < \lambda < 1450 \text{ \AA}$, and $f_\nu \propto \nu^{-1.5}$ for $\lambda < 1050 \text{ \AA}$. Hence, for the frequencies of interest, $f_\nu \propto \nu^{-\alpha_s}$ where $\alpha_s = 1.5$; the assumed spectral index is consistent with the inferred measurements (Wyithe & Bolton 2011) from observations of high-redshift quasar proximity zone sizes. These parameters are then used to derive the quasar contribution to the photoionization rates for H I, He I and He II respectively.

Since hydrogen is assumed to be highly ionized prior to the quasar being ‘switched on’, the H I ionization front from the quasar travels effectively at the speed of light. The region in the vicinity of the quasar in which the additional heating effects are expected to be significant may be characterized by the extent of the He III region. To calculate the extent of this region, we track the location of the He II ionization front. To do this, we use the relativistic equation of propagation of the ionization front modified to include the effects of optical depth:

$$\frac{dR}{dt} = c \left(\frac{\dot{N}_{\text{eff}} - 4\pi R^3 n_{\text{HeIII}} n_e \alpha_{\text{HeIII}} / 3}{\dot{N}_{\text{eff}} + 4\pi R^2 f_{\text{HeII}} n_{\text{He}} c - 4\pi R^3 n_{\text{HeIII}} n_e \alpha_{\text{HeIII}} / 3} \right) \quad (1)$$

where $\dot{N}_{\text{eff}} = \dot{N} e^{-\tau_{\text{HeII}}}$ with \dot{N} being the rate of production of He II-ionizing photons, and τ being the optical depth at the He II edge at the distance R . The above equation is analogous to that used by Icke (1979) for the case of stellar Stromgren spheres, in which the optical depth effects are incorporated. Using the above equation, we can compute the time required by the He II front to reach a particular gridpoint under consideration. We can also compute the distance R reached by the front after a time t_Q , where t_Q is the lifetime of the quasar. This distance $R_{\text{He}} = R(t = t_Q)$ is defined to be the location of the He II ionization front (or radius of the He III ionized sphere) at the end of the quasar lifetime. We use this distance R_{He} to quantify the extent of the region in which additional heating effects are expected to be important, later in Sec. 4.1.

Our numerical procedure is described in detail in Appendix A. For the evolution of the species densities and temperatures, we closely follow Bolton & Haehnelt (2007a). The radiative transfer implementation differs from Bolton & Haehnelt (2007a) as regards the tracking of the ionization front. We have validated the front locations and speeds with Fig. 5 of McQuinn (2012), and the effect of the front propagation on the size of the near-zones is described in Sec. 4.1.

2.2 Profile generation and statistics

We define the redshift grid along a line-of sight, using:

$$x(z) = \int_0^z d_H(z') dz' \quad (2)$$

where $d_H(z) = c(\dot{a}/a)^{-1}$ is the Hubble distance and a is the scale factor. Once we know the ion densities and gas temperatures at each pixel, following Choudhury, Srianand & Padmanabhan (2001), the Lyman- α optical depth due to hydrogen at every redshift z_0 can be computed as:

$$\tau_\alpha(z_0) = \frac{cI_\alpha}{\sqrt{\pi}} \int dx \frac{n_{\text{HI}}(x, z(x))}{b[x, z(x)][1 + z(x)]} \times V \left\{ \alpha, \frac{c[z(x) - z_0]}{b[x, z(x)](1 + z_0)} + \frac{v[x, z(x)]}{b[x, z(x)]} \right\} \quad (3)$$

where $b[x, z(x)] = \sqrt{2k_B T[x, z(x)]/m_H}$ is the thermal b -parameter for hydrogen, V is the Voigt profile function, in which the damping coefficient is $6.265 \times 10^8 \text{ s}^{-1}$, and $I_\alpha = 4.48 \times 10^{-18} \text{ cm}^2$ is related to the absorption cross-section σ_α for the Lyman- α photons:

$$\sigma_\alpha(\nu) = \frac{cI_\alpha}{b\sqrt{\pi}} V \left[\alpha, \frac{c(\nu - \nu_\alpha)}{b\nu_\alpha} \right] \quad (4)$$

where ν_α is the hydrogen Lyman- α frequency which corresponds to the wavelength 1215.67 Å. Using the above expression for the Lyman- α optical depth, the simulated spectra are generated using $F = \exp(-\tau_\alpha)$ for the flux F at each pixel.⁴ We mimic the noise by adding Gaussian distributed noise having a signal-to-noise ratio (SNR) 21, equal to a typical SNR achieved for $z \sim 6$ quasars with available instruments. We generate spectra for a number of such lines of sight for the statistical analyses. We consider two statistical indicators of the effect of the additional heating in this work : (a) the flux PDF statistics and (b) the curvature statistics. Note that Bolton et al. (2012) have used the cumulative distribution of velocity widths of Lyman- α lines obtained with Voigt profile fitting, to measure the temperature. However, unlike in the case of low redshift Lyman- α forest absorption, one will not be able to use higher Lyman-series lines to constrain the number of Voigt profile components. Hence, the derived b -distribution need not be well constrained. Therefore, in the present analysis, we explore the possibility of using the curvature statistics, that does not involve Voigt profile decomposition, to quantify the detectability of additional heating. Section 4.2 contains detailed descriptions of the flux and curvature statistics used to investigate the heating effect.

3 EXCESS HEATING IN THE QUASAR NEAR-ZONES

In this section, we describe a validation of the numerical procedure by computing the additional heating effect and comparing it to the measured value of the average excess temperature in the near-zones of quasars in Bolton et al. (2012). In particular, we investigate the effects of varying the normalization of the initial equation of state, and also the He II fraction in the vicinity of the quasar before the quasar is switched on. We explore how the combination of these parameters may be used to place possible constraints on the redshift

⁴ Though we do not convolve the spectra with instrumental broadening, this effect is expected to be negligible as compared to the thermal broadening effect which we are interested in.

of H I reionization as well as single-step reionization models where He II is also ionized by massive stars.

For this purpose, we employ the results of the $512^3, 10h^{-1}$ comoving Mpc box simulation with the quasar having a luminosity corresponding to $M_{\text{AB}} = -26.67$ at 1450 Å, and a lifetime of 100 Myr. The initial equation of state parameters and the background photoionization rates are varied and the resulting final values of temperature as a function of $(1 + \delta)$, where, δ is the overdensity, are computed.

3.1 Modifications to equation of state

In Fig. 1, we have plotted the $T - (1 + \delta)$ relation prior to and after additional heating by the quasar. We have chosen three different normalizations of the initial equation of state: $T_0 = 8000, 10000$ and 12000 K, keeping the slope $\gamma = 1.3$ fixed. The range in δ plotted is from low to mildly nonlinear overdensities, and is representative of the range that contributes significantly to the intergalactic Lyman- α absorption seen in quasar spectra. For each value of T_0 considered, the parameter $\Gamma_{\text{HeII}}^{\text{bg}}$ is varied from 10^4 HM12 to HM12, where HM12 ($= 4.42 \times 10^{-19} \text{ s}^{-1}$) is the value of the background He II photoionization rate computed by Haardt & Madau (2012). This is equivalent to varying the initial He II fraction in the vicinity of the quasar from $x_{\text{HeII}} \sim 0.05$ to $x_{\text{HeII}} \sim 1$. We first describe the basic trends which are apparent in all the figures:

(a) For all values of $\Gamma_{\text{HeII}}^{\text{bg}}$ under consideration, there is an increase in the temperature. When $\Gamma_{\text{HeII}}^{\text{bg}}$ is higher (i.e. the initial x_{HeII} is close to 0.05), the temperature enhancement is less. Also, irrespective of $\Gamma_{\text{HeII}}^{\text{bg}}$, the heated ‘equations of state’ approach each other at high densities where the effects of recombination keep the He II fraction high, and hence the gas is heated to a higher temperature. Therefore, for higher $\Gamma_{\text{HeII}}^{\text{bg}}$, the measured value of γ also becomes large (the ‘heated’ equation of state acquires a steeper slope).

(b) When $\Gamma_{\text{HeII}}^{\text{bg}}$ is very small (i.e. the initial x_{HeII} is close to 1), there is a uniform rise in temperature over the whole range of δ under consideration, i.e. we find a δ -independent heating. This leads to the equation of state being shifted upward (i.e. only enhancement in T_0) with a negligible change in the slope. If indeed a major part of He II is ionized at $z \sim 6$ by the quasars, then our findings suggest that the H I gas will still have some memory of the H I reionization.

To summarize, there are two simultaneous trends which occur in the equation of state due to the decrease in x_{HeII} : (a) a decrease in the normalization shift, and (b) an increase in the slope. We now consider these two trends separately, i.e. we explore the *individual* change in the parameters T_0 and γ (ΔT_0 and $\Delta\gamma$) when the value of x_{HeII} is changed.

For each initial value of T_0 (8000 K, 10000 K and 12000 K), we plot the change in temperature at the mean density, ΔT_0 against x_{HeII} for the five different values of x_{HeII} under consideration. This is shown in Fig. 2. It can be seen that $\Delta T_0 \propto x_{\text{HeII}}$ for all values of the initial T_0 . This is in line with the analytic formulation provided in Furlanetto & Oh (2008) where it is argued that $\Delta T \propto x_{\text{HeII}}$ (initial), where ΔT is the difference between the initial and heated temperatures. If we consider a fixed value of x_{HeII} , for a higher initial T_0 , the value of the ΔT_0 is lower. This, again, is consistent with our previous findings that regions which are already ‘heated’ can be additionally heated only to a limited extent.

We now investigate the corresponding relationship for the case of the change in γ , i.e. the $\Delta\gamma - x_{\text{HeII}}$ relation. For this, we plot the difference $\Delta\gamma$ between the slopes of the ‘heated’ and ‘initial’

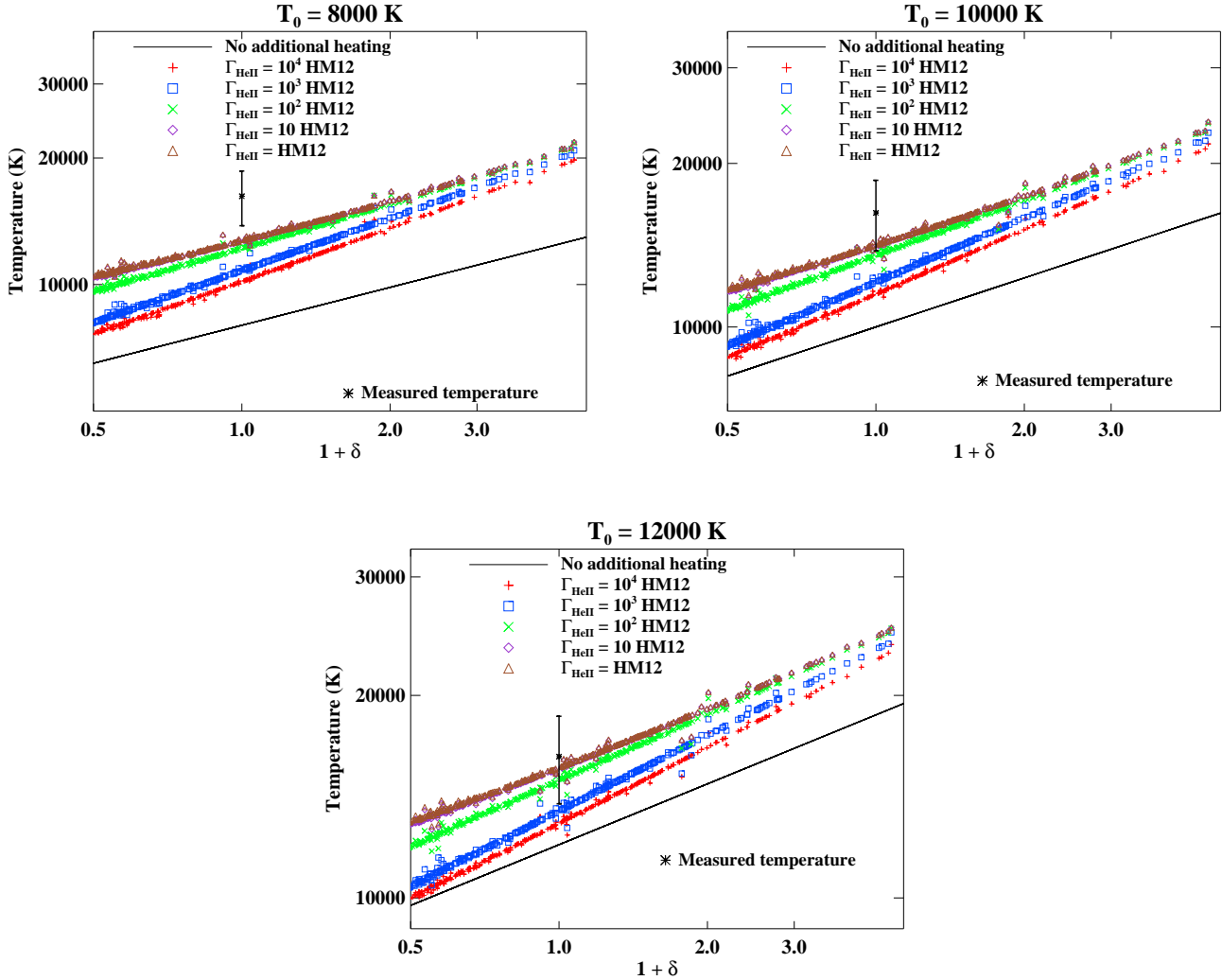


Figure 1. The initial equation of state and the effect of the additional heating for different values of the background metagalactic photoionization rate, $\Gamma_{\text{HeII}}^{\text{bg}}$ (in s^{-1}). The normalization of the equation of state, T_0 is varied from 8000 - 12000 K. For each value of T_0 , $\Gamma_{\text{HeII}}^{\text{bg}}$ is varied from 10^4 HM12 to HM12, where HM12 is the Haardt-Madau background photoionization rate. This is equivalent to varying the initial He II fraction in the quasar vicinity from $x_{\text{HeII}} \sim 0.05$ to $x_{\text{HeII}} \sim 1$. In each figure, the asterisk with the error bar shows the measured average temperature in the near-zones of the seven redshift ~ 6 quasars considered in Bolton et al. (2012).

equations of state, against x_{HeII} , for the five different values of x_{HeII} under consideration. This is done for each initial value of T_0 (8000 K, 10000 K and 12000 K). The results are shown in Fig. 3. As expected, there is negligible change in γ when the He II fraction is close to 1. We also note that for a fixed value of x_{HeII} , the value of $\Delta\gamma$ is higher when the initial T_0 is lower. However, we see that the value of $\Delta\gamma$ reaches a maximum of about 0.1 at the lowest He II fraction and initial T_0 that we consider. The reason for this flattening is as follows: At high enough densities, all the curves in Fig. 1 are constrained to follow the top curve due to recombination effects. At lower values of density, each curve in Fig. 1 is shifted upward with respect to the initial equation of state, and the magnitude of this shift increases with increase in the value of x_{HeII} . However, for low enough values of x_{HeII} , both the ‘right top point’ (which is constrained due to recombination effects) and the ‘left bottom point’ (which is anchored close to the initial equation of state) are asymptotically fixed. This brings the slope to a near-saturation, which leads to the flattening out of $\Delta\gamma$. The max-

imum change in slope is greater if the shift in the overall normalization is higher, which happens if the initial T_0 is lower. Hence, the maximum value of $\Delta\gamma$ decreases with increase in the initial T_0 , as we see in Fig. 3. Our $\Delta\gamma - x_{\text{HeII}}$ relation above is analogous to the $\Delta T - x_{\text{HeII}}$ noted in the literature. We infer that the value $\Delta\gamma \sim 0.1$ is representative of the maximum increase in the slope of the equation of state that may be achieved in physically feasible reionization scenarios.

We speculate that the shifting upwards of the equation of state (which arises when the initial x_{HeII} values are high), may be easier to detect observationally than the (maximum) slope change of $\gtrsim 0.1$ (which occurs when the initial x_{HeII} values are low). This also depends on how sensitive the statistical test used for distinguishability, is to the steepness of the equation of state, as compared to how sensitive it is to an overall increase in normalization. We will find, in the subsequent sections, that the curvature statistic is more sensitive to the expected shift $\Delta T_0 \sim 1000 - 5000$ K in the

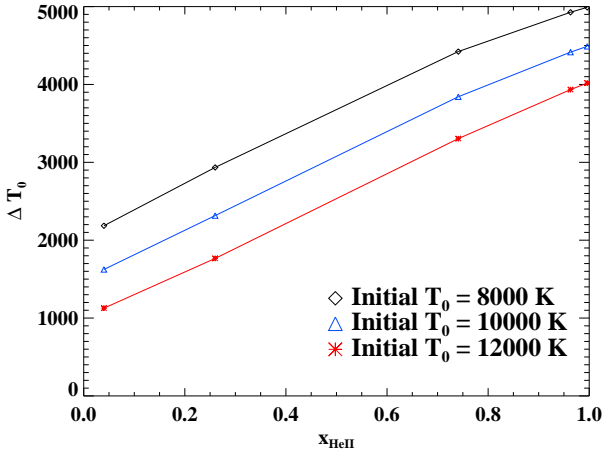


Figure 2. The variation of ΔT_0 with the initial x_{HeII} . The relationship is linear, with the ΔT at a fixed x_{HeII} increasing with decrease in initial temperature.

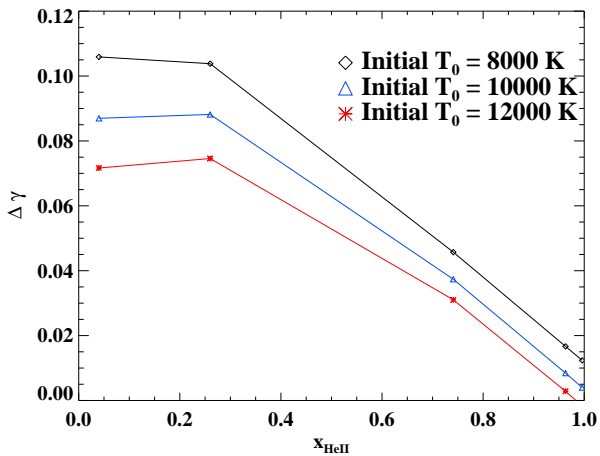


Figure 3. The variation of $\Delta\gamma$ with the initial x_{HeII} . The $\Delta\gamma$ at a fixed x_{HeII} increases with decrease in initial temperature, but reaches a maximum of about 0.1 at the lowest He II fractions under consideration.

normalization of the equation of state, than to the expected change $\lesssim 0.1$ in its slope.

3.2 Implications of temperature measurements

We now compare the results of our simulations with the available observations. At present, with a limited number of $z \sim 6$ quasars that are observed at high spectral resolution, constraints on the slope of the equation of state may be difficult. However, T_0 can be measured (see Bolton et al. 2012). In what follows, we try to get constraints on the $\Gamma_{\text{HeII}}^{\text{bg}}$ using the available T_0 measurements. The measured average temperature ($\log T$ (in K) = $4.21_{-0.07}^{+0.06}$) in quasar near-zones at redshift ~ 6 (Bolton et al. 2012) is indicated by the asterisk with error bar in each plot of Fig. 1. We note the following:

(a) If the initial equation of state has $T_0 = 8000$ K (a lower initial temperature), then the temperatures are lower than the 1σ

lower bound on the measurement for all the $\Gamma_{\text{HeII}}^{\text{bg}}$ values under consideration. Thus it may be possible to rule out the corresponding reionization histories leading to this temperature prior to the switching on of the quasar. The temperature $T_0 = 8000$ K arises, for example, if we assume the instantaneous reionization followed by adiabatic cooling and compression, when the redshift of reionization of hydrogen is at $z_{\text{re}} = 11$ with its associated temperature being $T_{\text{re}} \sim 25000$ K.

(b) However, if the initial $T_0 = 10000$ K, then the $\Gamma_{\text{HeII}}^{\text{bg}}$ is constrained to $\lesssim 10^{-18} \text{ s}^{-1}$, which corresponds to $x_{\text{HeII}} \gtrsim 0.96$, in order to be consistent with the measurements. The value of $T_0 = 10000$ K is, in turn consistent, with the reionization of H I at $z_{\text{re}} = 11$ and $T_{\text{re}} \sim 30000$ K. These are physically acceptable redshifts and temperatures of H I reionization.

(c) If the initial equation of state, on the other hand, has $T_0 = 12000$ K (a higher initial temperature), then the $\Gamma_{\text{HeII}}^{\text{bg}}$ value is constrained to $\lesssim 10^{-16} \text{ s}^{-1}$, which corresponds to $x_{\text{HeII}} \gtrsim 0.26$, in order to be consistent with the measured temperature. The values of the initial $T_0 = 12000$ K and $\gamma = 1.3$ are difficult to reproduce with simple reionization models involving only adiabatic cooling and compression, but may arise in more complex models involving external sources of heating etc. In this case, the temperature measurement may be consistent with single-step models of reionization. It is to be noted that the additional heating effect is smaller for the case of higher initial T_0 than for the lower case. This leads to the curves being closer to each other in the bottom panel of Figure 1. In fact, this effect can be quantified using the curvature statistics by performing a Kolmogorov-Smirnov test between the ‘initial’ and ‘heated’ spectra, which we do and describe further in Section 4.2.

In this way, the exercise presented above validates our procedure and also captures the dependence of the heating to (a) T_0 , which connects up the heating effect to the epoch of hydrogen reionization in two-step models, and (b) $\Gamma_{\text{HeII}}^{\text{bg}}$, which connects to the possibility of single-step reionization of both H I and He II. In any case, the prevalence of sufficiently hard sources at high redshifts substantially increases the $\Gamma_{\text{HeII}}^{\text{bg}}$ value and hence affects the temperature in the near-zone. In the following sections, we quantify each of these effects, and also relate them to the *detectability* of the additional heating using statistical analyses.

4 RESULTS

In the previous section, we have described in detail the modifications to the equation of state that occur due to the effect of the additional heating. We have also investigated the implications of the measured temperature in the near-zones of the quasars on the values of the various parameters of the IGM at that epoch. These point to constraints on both, the epoch of reionization of H I as well as single-step models of reionization. In the present section, we shall describe the main results of our simulations with respect to : (a) the relative extent of the He-heated region around quasars, compared to the H I proximity zone, as a function of the age of the quasar, (b) the detectability of the additional heating effects as quantified by the flux and curvature statistics, and (c) implications for the detectability of additional heating in single-step reionization scenarios.

4.1 Extent of additional heating around quasars

As the Lyman- α absorption from the general IGM at redshift 6 is optically thick, a profile analysis to estimate the gas temperature

can be performed only in the quasar’s proximity zone. In this zone, the H I gas is highly ionized due to the excess ionization from the quasar. However, the fraction of this gas which is influenced by additional heat from the He II ionization by the quasar depends on where the He II front is located. This depends both on the quasar lifetime t_Q , as well as the line-of-sight optical depth for the He II ionizing photons. If the He III front does not reach the edge of the H I proximity zone for some reason, it would lead to dilution in the statistical tests to measure excess temperature. In order to provide estimates on the front location and the H I proximity zone, a larger box-size (which includes these regions which are typically of the order of 8-9 proper Mpc) is required. Therefore, in this section, we address this issue using the lower resolution 256^3 , $60h^{-1}$ comoving Mpc box simulation with the initial equation of state having $T_0 = 10^4$ K, $\gamma = 1.3$, and the quasar luminosity corresponding to $M_{AB} = -26.67$ at 1450 \AA .

Using Eq. (1), the equation of propagation of the He II ionization front that takes into account optical depth effects, we calculate the location $R_{\text{He}} = R(t_Q)$ of the front at the end of the quasar lifetime t_Q . The He II front location is computed for 50 random lines-of-sight extracted in the simulation box. We repeat the computation for two different values of t_Q , 10 Myr and 100 Myr⁵, and the results are plotted in Fig. 4. It can be seen that the extent of the He III region (where additional heating of He, etc. are expected to be significant) increases as the quasar lifetime is increased, going up to about 8-8.5 proper Mpc from the quasar in a time interval of 100 Myr. The blue vertical line shows the maximum extent of the He III region for a given t_Q which occurs in the limit of zero optical depth. This is computed by setting $\tau_{\text{HeII}} = 0$ in Eq. (1), so that $\dot{N}_{\text{eff}} = \dot{N}$, where \dot{N} is the rate of production of ionizing photons from the quasar. For quasar lifetimes of the order of 10 Myr, the optical depth effects are negligible and the mean location of the front is close to the maximum value that occurs in the limit of zero optical depth. For $t_Q \sim 100$ Myr, the front is able to travel a greater distance, but the optical depth effects begin to be important, and, on an average, the front reaches $\gtrsim 80\%$ of the maximum distance in about 66% cases.

We now consider the relative extent of the He III region with respect to the H I proximity zone of the quasar. Since one looks for the signatures of additional heating in the full H I proximity zone of the quasar, it is important to quantify the extent of the region within this proximity zone in which additional heating effects due to ionization of He II are significant. The H I proximity zone, R_{H} , is defined through the relation $\Gamma_{\text{HI}}^{\text{QSO}}(R_{\text{H}}) = \Gamma_{\text{HI}}^{\text{bg}}$. The maximum value of R_{H} for the quasar luminosity under consideration and the background $\Gamma_{\text{HI}}^{\text{bg}}$, is ~ 14 proper Mpc from the quasar. The distance R_{He} is defined as $R_{\text{He}} = R(t = t_Q)$ using Eq. (1) with the optical depth effect taken into account. The ratio $R_{\text{He}}/R_{\text{H}}$, representing the relative extent of the He III region within R_{H} , is plotted as histograms in Fig. 5 for the 50 lines-of-sight considered. It can be seen that this ratio is about 30 – 35% for quasar lifetimes of the order of 10 Myr, but increases to about 80% for a quasar lifetime of ~ 100 Myr. This illustrates that the He II front covers about 80% of the H I proximity zone of the quasar for $t_Q \sim 100$ Myr.

The above result is closely connected with a related phenomenon of the “saturation” or equilibrium value of the temperature in the region in which the heating effect is important. This

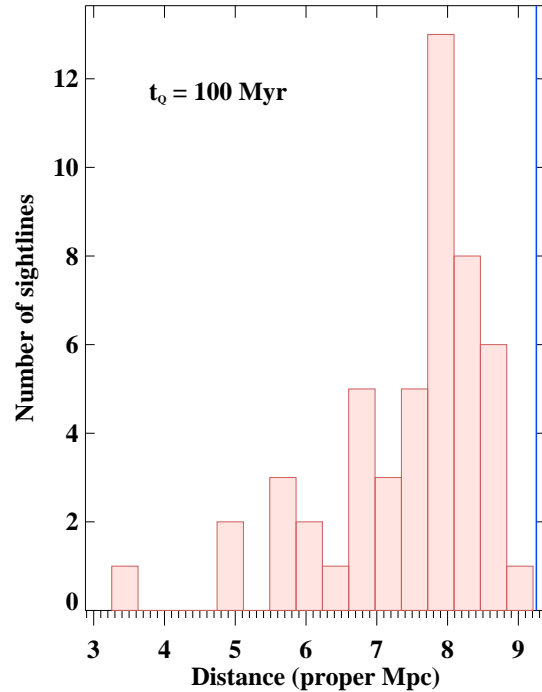
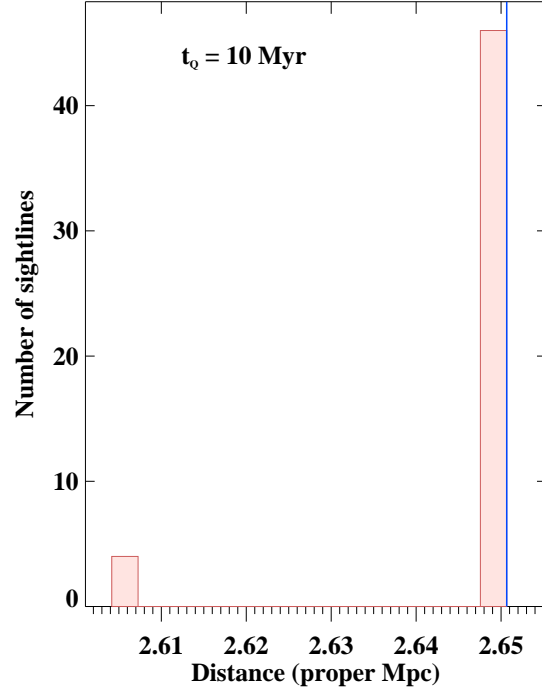


Figure 4. The extent of the He III zone R_{He} for quasar lifetimes of 10 Myr (top panel), and 100 Myr (bottom panel). Each histogram comprises a total of 50 lines-of-sight. The blue vertical line shows the location of the He II front when the effect of optical depth is neglected, which represents the maximum extent of the He III region for the given time.

⁵ The assumed lifetimes of the quasar considered are indicative; at redshifts $z \sim 6$, measurements have placed the lifetimes of quasars at $\geq 10^7$ years (Haiman & Cen 2002; Walter et al. 2003).

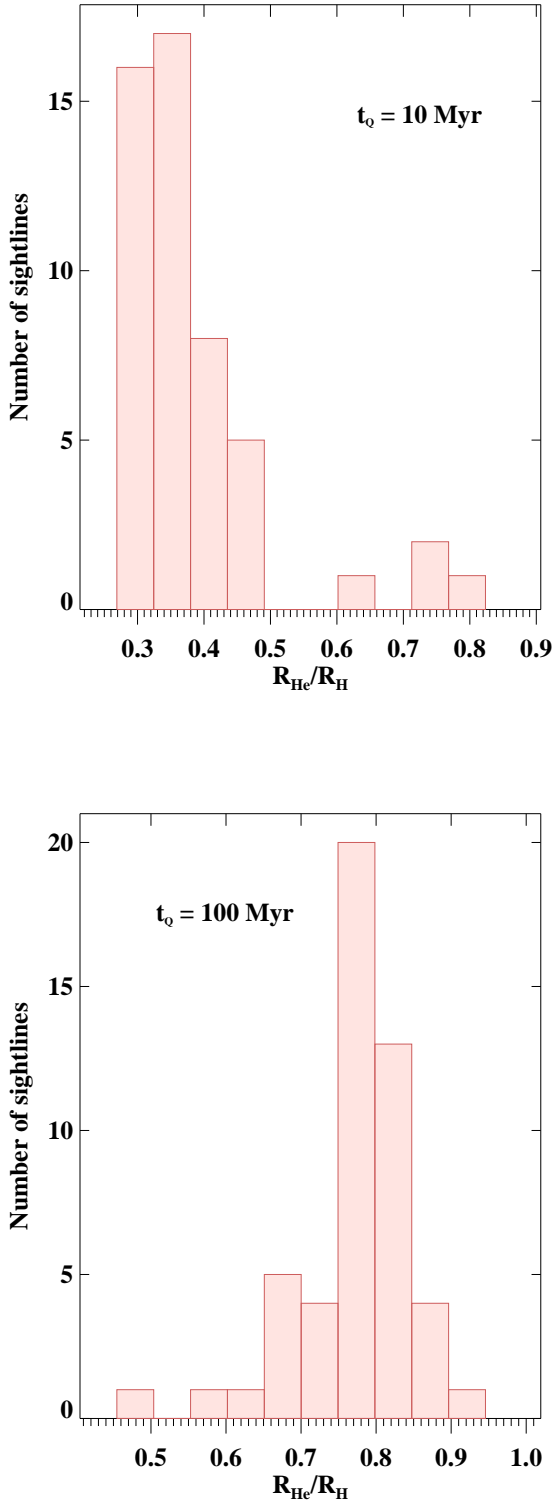


Figure 5. The *relative* extent of the He III zone with respect to the H I proximity zone, $R_{\text{He}}/R_{\text{H}}$, for quasar lifetimes of 10 Myr (top panel), and 100 Myr (bottom panel). Each histogram comprises 50 lines-of-sight. As the quasar lifetime is increased, the relative extent of the He III region also increases. For $t_Q \sim 10^8$ years (the typical inferred lifetime of the $z \sim 6$ quasar), more than 80% of the H I proximity zone is heated in 78% of the sightlines.

saturation effect is seen as an increase in the temperature in a fairly distance-independent manner so that an equilibrium value is reached, after which there is little or no increase in the temperature over the timescales of interest for almost all gridpoints in the He III region under consideration. This places a maximum bound on the temperature which the IGM may be heated to with ionization of both H I and He II. This effect is reminiscent of the corresponding phenomenon in the interstellar medium where one finds the maximum temperatures to be $T_{\text{HI}} \sim 20000$ K when H I is ionized and $T_{\text{HeII}} \sim 40000$ K when both H I and He II are ionized; the exact values vary according to the detailed physics and optically thick/thin cases, but these numbers provide reasonable upper limits. In our present case the saturation is found to be achieved when the lifetime of the quasar is sufficiently high, ~ 100 Myr. Since the helium front covers about 80% of the H I proximity zone within this time, the additional heating effect extends into a larger region and consequently, the rise in temperature is much more apparent, and fairly independent of distance. In contrast, for a quasar lifetime of 10 Myr, only about 30 – 35% of the H I proximity zone near the quasar is influenced by the additional heating and it is possible that some of the pixels inside these regions have not yet reached the saturation in temperature. This means that for sufficiently long time scales (~ 100 Myr), the additional heating depends more on the initial IGM parameters and less on the distance from the quasar and the gas density. This turns out to be important for the discussion in the following sections.

4.2 Flux statistics and dependence on equation of state

In this section, we will explore some statistical tests to understand the sensitivity of the additional heating effect to the parameters of the general intergalactic medium at that epoch. For this purpose, we use the results of 512^3 simulation box, which has a resolution of 2.65 km/s per pixel, and consider a quasar having a luminosity corresponding to $M_{\text{AB}} = -26.67$ at 1450 \AA , and a lifetime of 100 Myr. We consider two statistics which are both based on the observed hydrogen Lyman- α spectrum in order to quantify the additional heating effect, and the dependence on the equation of state parameters, T_0 and γ : (a) the probability distribution function (PDF) of the flux, and (b) the PDF of the flux curvature. We also consider the two-dimensional flux-curvature distribution. We probe cosmic variance by using the same set of parameters, but different sets of lines-of-sight.

The fiducial equation of state used for this purpose is $T_0 = 10^4$ K, $\gamma = 1.3$. The background $\Gamma_{\text{HI}}^{\text{bg}}$, $\Gamma_{\text{HeI}}^{\text{bg}}$ and $\Gamma_{\text{HeII}}^{\text{bg}}$ values correspond to those given by HM12 (Haardt & Madau 2012) at redshift 6. The transmitted flux in the Lyman- α forest is sensitive to both, the temperature as well as the ionization state of hydrogen and therefore, to isolate the effect of additional heating around the quasar, we require the breaking of this degeneracy. For our chosen background photoionization rates, the spectrum when the quasar is not present is dark and hence featureless at redshift 6. Hence, it is impossible to compare the flux obtained from this spectrum with that when the quasar is present. Hence, we instead isolate the heating effect by generating a control sample (with the same initial conditions) of spectra with the temperature given by the initial equation of state and the ionization state being the same as that when the quasar is present. In other words, there is no He-related heating in the “control” sample. Gaussian distributed noise is added to both the “control” and the “heated” spectra with a signal-to-noise ratio 21, mimicking the typical values in the observed HIRES quasar spectra.

For all the statistical analyses, we replicate the typical sample size (total number of pixels) used in the observational studies of the $z \sim 6$ quasars till now, since the spectral resolution in the observations is close to the resolution in our simulations. To take into account any distance-dependent effects, it may also be desirable to use a longer line-of-sight obtained by splicing together shorter sightlines available in the simulation box. However, we have seen in the previous section that for quasar lifetimes of the order of 100 Myr, the temperatures reach equilibrium and the heating effect becomes fairly independent of distance from the quasar. To illustrate this statistically, we implemented the numerical routine for the fiducial equation of state parameters, $T_0 = 10^4$ K and $\gamma = 1.3$ for a line-of-sight having length $40h^{-1}$ comoving Mpc (constructed by splicing together four lines-of-sight of length $10h^{-1}$ comoving Mpc each having 512 pixels), with the quasar lifetime of 100 Myr. The generated sample spectra, both heated (red) and control (black) are plotted in Fig. 6. Five such lines-of-sight were considered (so that the total sample size, (2048×5) pixels \times 2.65 km/s per pixel ~ 7 quasars \times 3500 km/s per quasar), and the flux PDF was generated for both the heated and the control spectra. The flux PDFs for the control and the heated sample were compared using the Kolmogorov-Smirnov (KS) statistic, and they were found to be distinguishable with 94.5% confidence.

This shows that the distinguishability of the samples is fairly independent of distance from the quasar if the quasar lifetime is of the order of 100 Myr. We also noticed that the temperature enhancement is fairly independent of the distance of the pixel from the quasar, for this case. On the other hand, if the same exercise is repeated for a quasar lifetime of 10 Myr, it is found that the sample with additional heating resembles the control sample very strongly and the two flux PDF distributions are distinguishable only at the 15% level. This is to be expected since, as we have seen in Sec. 4.1, the helium front travels to only about 30 – 35% of the hydrogen near-zone in this lifetime and hence the additional heating effect is confined to a small part of the line-of-sight under consideration.⁶

We thus infer that for sufficiently long timescales of ~ 100 Myr, the actual location of the pixel with respect to the quasar may not be as relevant as other parameters such as the initial equation of state as far as the heating effect is concerned. For this reason, in all the further statistical studies, we will use 20 lines-of-sight of length $10h^{-1}$ Mpc each comprising 512 pixels, which replicates the sample size in the observations of the quasar spectra⁷.

4.2.1 Flux PDF statistics

We compare two samples of 20 lines-of-sight each having 512 pixels⁸ for the “control” and “heated” spectra generated, using the

⁶ It is assumed that the quasar shines with constant flux during the entire lifetime for the purpose of the simulations. For long timescales (\gtrsim few Myr), the quasar light curves cannot be constrained using direct observations. However, these and subsequent results depend upon the integrated thermal effects throughout the active lifetime of the quasar. The luminosity of the quasar used in the simulations is to be taken an estimate of the average luminosity of the quasar throughout its active lifetime.

⁷ We are not concerned with the spatial density correlations in the present study.

⁸ Due to the limited box size of the simulation, about 20 pixels at the extreme of the box have slight errors in the Lyman- α optical depth due to the incompleteness of the integral in the Voigt profile generation. For the statistical tests, therefore, we discard these 20 pixels (equivalent to about 50 km/s) at the extreme of the box.

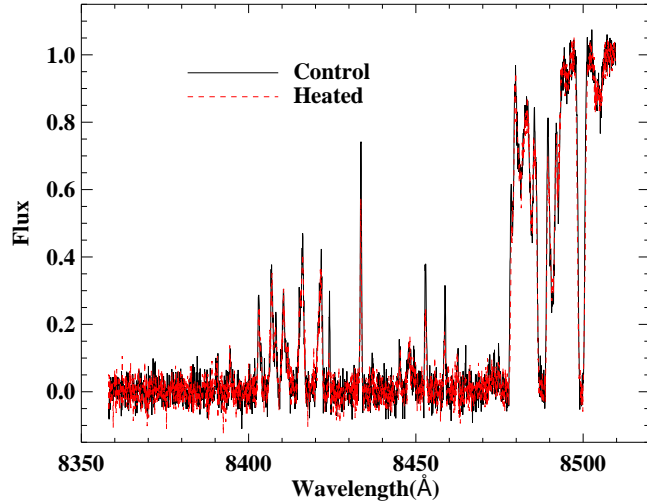


Figure 6. Sample spectra, both heated (red dashed line) and control (black solid line) for a line-of-sight having 2048 pixels drawn through the simulation box. The quasar lifetime is 100 Myr and the flux PDFs of the two samples are distinguishable with 94.5 % confidence.

Kolmogorov-Smirnov (KS) statistic. Note that apart from the additional heating, all other parameters of the heated model are identical to the “control” one. The results for the cumulative flux distributions are plotted below in Fig. 7 and Fig. 8, along with the KS statistics ‘ d ’ (the maximum separation between the two cumulative probability distributions) and ‘prob’ (the probability that the two samples come from the *same* parent distribution) in each case. In Fig. 7, the temperature at mean density is fixed at $T_0 = 10^4$ K and γ is increased from 1.1 to 1.5. It can be seen, that the distributions for the samples with and without additional heating may be distinguished with $\sim 100\%$ confidence when $\gamma = 1.1$, but only with 69.78% confidence when $\gamma = 1.5$. Hence, a higher slope of the initial equation of state leads to a greater resemblance to the control sample. In Fig. 8, the slope is fixed at $\gamma = 1.3$ and T_0 is varied from 8000 K to 12000 K. The flux PDFs for the sample with and without additional heating are distinguishable at the 99.79% level when $T_0 = 8000$ K, but only at the 87.13% level when $T_0 = 12000$ K. Hence, if the initial T_0 is larger, the distinguishability of the two samples becomes poorer.

We conclude that we are able to distinguish between the heated and control samples using 20 lines-of-sight and the flux PDF, and the extent of the distinguishability is sensitive to the initial parameters (T_0 and γ) of the equation of state. However, among these 20 lines-of-sight, we find that the statistical difference in the inferred flux PDF due to cosmic variance is greater than the difference introduced by additional heating from the quasar. This is summarized in Fig. 9 where we have plotted the cumulative probability distribution for two subsamples each from the control and the heated distributions. Each sample comprises 5120 pixels (10 lines-of-sight). It can be seen that the effect of additional heating on the flux PDF is within the cosmic variance of the individual samples. Hence, we infer that the flux PDF alone is not very sensitive to the additional heating effect, but may be more sensitive to the H I ionizing radiation, which is the purpose for which it is traditionally used.

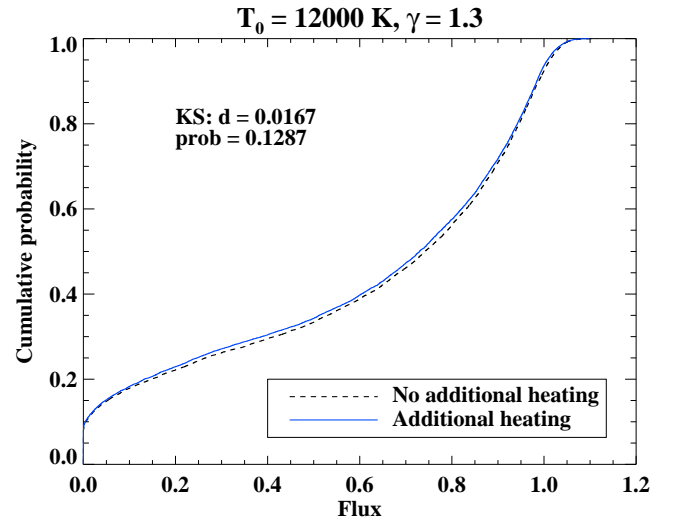
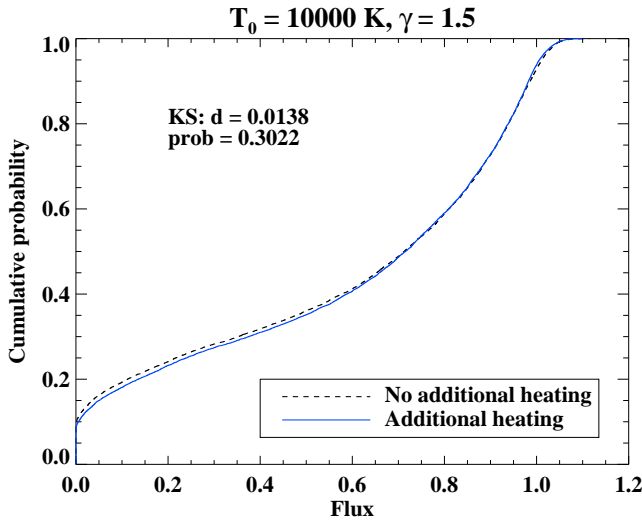
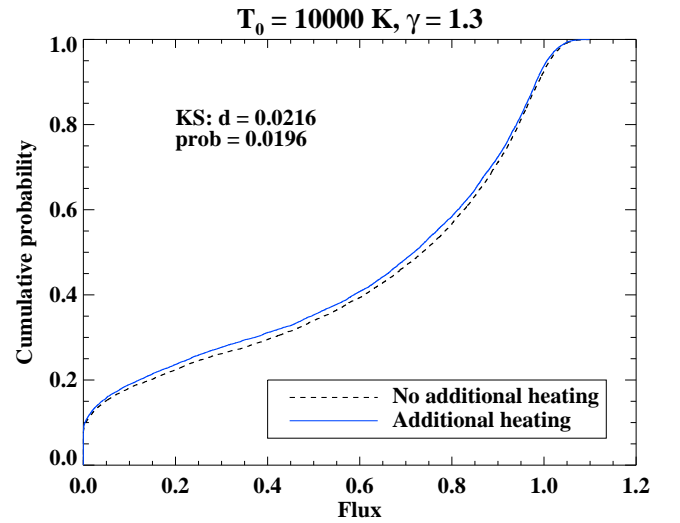
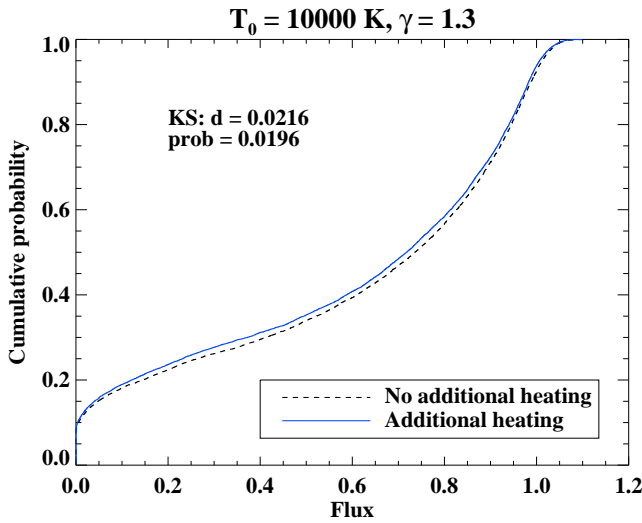
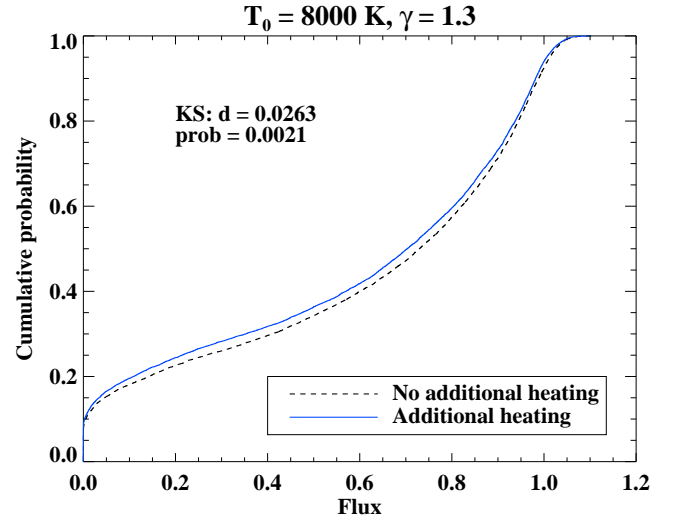
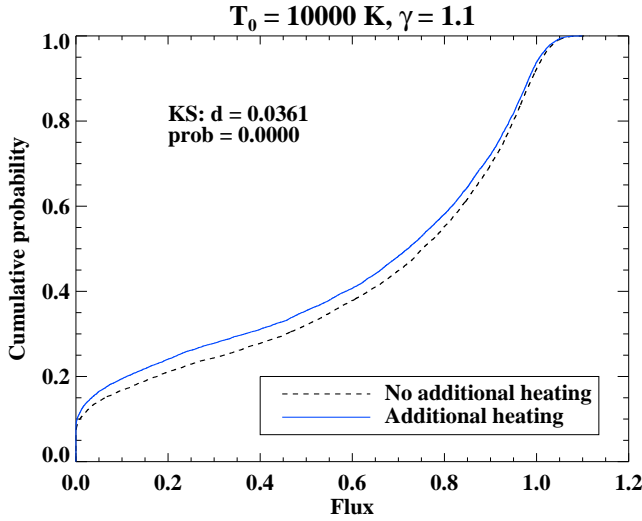


Figure 7. Comparison of the cumulative flux PDF of the spectrum with and without additional heating by the quasar for a sample of 20 lines-of-sight each having 512 pixels, drawn through the simulation box. The temperature at mean density is taken as 10^4 K with the slope being varied from 1.1 (top), 1.3 (middle) and 1.5 (bottom). The values of the KS statistics d and prob are indicated on each panel. It can be seen that the distinguishability of the heated and non-heated spectra goes down as the slope of the equation of state is increased. With the smallest slope of 1.1, the spectra for the two cases are completely distinguishable even with 20 lines-of-sight.

Figure 8. Same as Figure 7, with the temperature at mean density being varied from 8000 K (top), 10000 K (middle) and 12000 K (bottom). The distinguishability of the heated and non-heated spectra goes down as the value of the temperature at mean density is increased. With the smallest temperature of 8000 K, the spectra for the two cases are distinguishable at the 99.79% level even with 20 lines-of-sight.

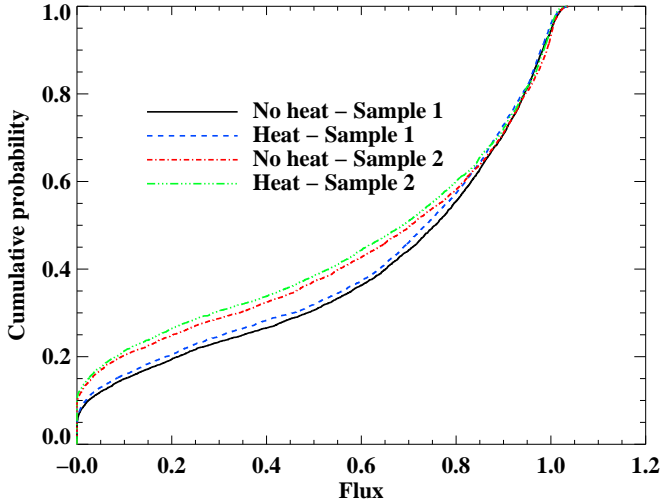


Figure 9. The cumulative probability distribution of the flux, for two samples each of control and heated spectra. Each sample comprises 10 lines-of-sight (5120 pixels). The blue dashed and green dot-dot-dashed curves represent the heated samples and the black solid and red dot-dashed curves represent the control ones. It can be seen that the effect of the additional heating is within the cosmic variance of the individual samples.

4.2.2 Curvature statistics

The flux PDF statistic points to a connection between the heating effect and the initial equation of state. However, the difference is within the individual cosmic variance of the samples, making it difficult for the technique to be used in practice to identify a given spectrum as being “heated” or not. In order to address this effect and also to isolate the effect of the additional heating from the ionization information (both of which are captured in the flux), we consider here an alternative statistic, to characterize the spectra. In the literature, this has been done in several ways: (a) by using the b -distribution from Voigt profile fitting to the mock spectra (e.g. Bolton et al. 2012), (b) by using wavelets (e.g. Theuns & Zaroubi 2000) or (c) by using the curvature parameter (e.g. Becker et al. 2011). Unlike in the case of low-redshift Lyman- α forest absorption, the b parameter need not be well constrained as one will not be able to use higher Lyman series lines. In this section, we explore the usage of the curvature parameter, to analyse the heating effect statistically. Following Becker et al. (2011), the curvature parameter can be defined as:

$$\kappa = \left| \frac{F''}{(1 + (F')^2)^{3/2}} \right| \quad (5)$$

where F is the normalized flux⁹. The binned average of the curvature at a given flux, together with simulations, are used to measure the IGM temperature without resorting to Voigt profile fitting techniques by Becker et al. (2011). As pointed out by these authors, the denominator of the above expression is essentially unity and hence only the double derivative of the flux contributes to the curvature. We follow Becker et al. (2011) where the flux (and all its derivatives) are measured with respect to the velocity grid in km/s.

⁹ Our κ corresponds to $|\kappa|$ of Becker et al. (2011).

	No noise	With noise
Flux	0.752	0.316
κ	0.002	0.768
2d KS test	0.021	0.529

Table 1. This table indicates the KS test probabilities for the non-noise added and the noise added spectra. The KS test is performed between the control and the heated samples of 512 pixels each. The last row indicates the probability values for the two-dimensional KS test of the flux- κ joint distribution. It can be seen that noise significantly affects the value of prob for the curvature statistic.

We evaluate the curvature parameter for both, the control and the heated spectra. In addition to the KS statistic for the flux, described in the previous subsections, we now also use the KS statistic for the κ distribution and use the two dimensional KS statistic to compare the joint flux- κ distributions. In this way, the effect of the additional heating may be quantified.

We begin by calibrating the effect of the curvature statistic. To do this, we consider the fiducial equation of state, having parameters $T_0 = 10^4$ K, $\gamma = 1.3$, and a single line-of-sight (512 pixels). We first generate noise-free spectra along the line-of-sight for both “control” and “heated” cases, and compute the curvature values for both of these. Noise is then added to both the control and heated samples, and the curvature values are again computed. Now, the control and the heated samples are statistically compared (using the KS test) with respect to the flux PDF, the curvature, and the joint flux- κ distributions for both the cases, i.e. with and without noise added to the spectra.

We find that when no noise is added to either the “control” or the “heated” spectra, then the three KS probabilities are 0.752 (for flux PDF alone), 0.002 (for κ alone¹⁰) and 0.021 (for the 2d KS test). This confirms that the curvature parameter is far better able to distinguish between the heated and the control samples than the flux PDF. This is to be expected since the curvature parameter directly captures the effect of thermal broadening.

On the other hand, when noise is added to both the “control” and “heated” spectra, then the above three probabilities become 0.316 (for flux PDF alone), 0.768 (for κ alone) and 0.529 (for the 2d KS test). These values (also summarized in Table 1) indicate that the curvature statistic is strongly influenced by the noise in the spectrum, which washes out the distinguishability of the control and the heated spectra. This has also been noted previously by Becker et al. (2011).

Since the noise significantly dominates the curvature statistic, in order for the efficient usage of the curvature statistic, it is important to smooth the noisy spectrum before applying this statistic. In Becker et al. (2011), this is achieved by fitting the raw spectra with a smoothly varying b -spline and the curvature is computed from the smoothed spectra. In this work, we convolve the noisy spectra with a Gaussian filter having a specific smoothing velocity width and vary the width until the convolved spectrum best matches the ideal, non-noise added spectrum. The results of this exercise are illustrated in Figs. 10 and 11. In Fig. 10, the top panel shows the 2D scatter plot of the κ -flux joint distribution for the control

¹⁰ Here, and in what follows, we disregard the pixels having flux values greater than 0.9 or less than 0.1, for all curvature statistics. This is done following Becker et al. (2011), to avoid both, saturated pixels at low flux as well as uncertainties in the curvature values at high flux.

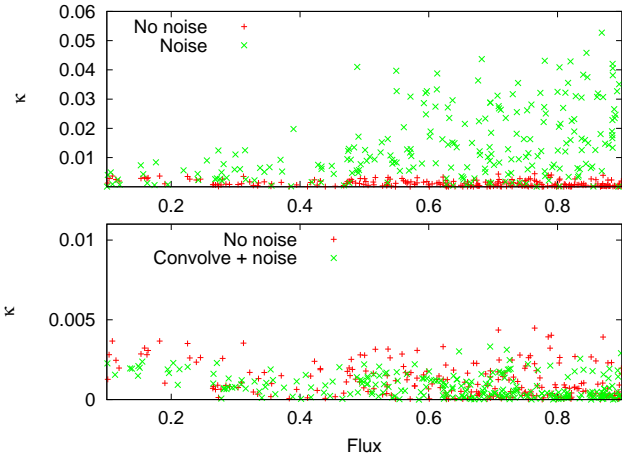


Figure 10. The top panel shows the 2D scatter plots of the flux- κ distribution in the non-noise added (ideal) case (red plus signs), and the noise added case (green crosses). The distributions are significantly different. In the bottom panel, the non-noise added (ideal) distribution (red plus signs) is shown along with the noisy spectrum convolved with a 10 km/s filter (green crosses). The figure shows that it is indeed possible to approach the ideal 2D distribution when the noise is convolved out with a smoothing velocity.

sample, with and without noise added to the spectrum. The bottom panel shows the noisy 2D distribution convolved with a Gaussian smoothing filter of 10 km/s, compared to the noise-free distribution. The figure shows that the noise is efficiently convolved out by smoothing with the Gaussian filter, since the convolved scatter plot closely resembles the original, non-noise added plot. We now fine-tune the value of the smoothing velocity until the convolved distribution most closely matches the ideal non-noise added distribution, and plots for different smoothing velocities of 3, 5, 7 and 8 km/s are in Figure 11. It is seen that a smoothing velocity of 7 km/s most closely matches the non-noise added distribution and hence we adopt it for the subsequent analysis. This is also apparent from the plot in Fig. 12 which illustrates the pixel dependence of the flux and the curvature parameter for the three cases : no noise, noise added, and noise convolved with the 7 km/s Gaussian filter. We also note that the curvature parameter values we obtain are consistent (at the same order-of-magnitude) with those in Becker et al. (2011)¹¹.

We now vary the equation of state, and the 2d KS test between flux and κ for 512 pixels (1 line-of-sight) yields the values in the second column of Table 2. It can be seen that the trend of greater distinguishability with smaller T_0 and γ , which we found for the flux PDF case, is reproduced for the case of the curvature statistic as well. The curvature statistic can effectively distinguish between the control and heated spectra for different equations of state even with a sample of 512 pixels (a single line-of-sight). The prob values for a sample of five lines-of-sight are also provided in the last column of Table 2. This shows that the distinguishability of the samples crosses the 90% level with a sample of 5 sightlines (equivalent to using two quasar spectra) for all equations of state under consideration. If we use 20 lines-of-sight, the control and heated

¹¹ As an aside, we have found that smoothing with a moving boxcar distribution for different boxcar widths does not produce the systematic effects noted in Fig. 11 and hence, the convolution with the Gaussian filter is preferred over the moving boxcar to smooth the distribution.

T_0, γ	2d KS prob (1 line-of-sight)	2d KS prob (5 lines-of-sight)
10^4 K, 1.1	0.067	3.326×10^{-9}
10^4 K, 1.3	0.146	8.955×10^{-5}
10^4 K, 1.5	0.801	0.093
0.8×10^4 K, 1.3	0.071	1.936×10^{-9}
1.2×10^4 K, 1.3	0.323	0.016

Table 2. This table indicates the two-dimensional KS test probabilities of the flux- κ joint distribution for different equations of state with a sample of 512 pixels (1 line-of-sight) and 2560 pixels (5 lines-of-sight). The KS test is performed between the control and the heated samples. It can be seen that the distinguishability of the samples decreases as T_0 and/or γ are increased, quantifying the dependence of the additional heating effect on the initial equation of state. Note that all the background photoionization rates are fixed at the HM12 values.

spectra are completely distinguishable (to less than about one part in 10^8) for all equations of state under consideration.

In order to explore the extent of the effect of cosmic variance on our results, we consider now our fiducial equation of state and compare the cumulative probability distributions of the curvature statistic for two control subsamples, each of 10 sightlines, and two “heated” subsamples, each again of 10 sightlines. The resulting plot is shown in Fig. 13. The blue dashed and green dot-dot-dot-dashed curves represent the heated samples and the black solid and red dot-dashed curves represent the control samples. It may be clearly seen that the heating effect is well above the “cosmic variances” of the individual samples; this figure may be compared to the previous Fig. 9 where the opposite effect was noted. Hence, we conclude that the curvature statistic will be able to distinguish the “non-heated” and “heated” spectra over and above their internal cosmic variance even when we use a sample size as limited as what is available today.

4.3 Dependencies on single-step reionization by Population III stars

In the preceding sections, we have statistically quantified the dependence of the heating effect on the equation of state parameters (T_0 and γ). In standard two-step reionization scenarios, these two parameters may be mapped to the redshift of hydrogen reionization, and the associated IGM temperature at that redshift. In this section, we briefly consider the effects of our study on constraining single-step models of reionization.

In Sec. 3, we illustrated the effects of changing the $\Gamma_{\text{HeII}}^{\text{bg}}$ photoionization rate on the temperature-density distribution, for different initial values of the normalization of the equation of state, T_0 . We also indicated which combinations of these two parameters produced results which were consistent with those measured in the near-zones of the $z \sim 6$ quasars (Bolton et al. 2012). It was found that when the $\Gamma_{\text{HeII}}^{\text{bg}}$ was small (or when the initial x_{HeII} was high), T_0 showed the maximum increase with no apparent change in γ . However, as the $\Gamma_{\text{HeII}}^{\text{bg}}$ became higher, while the increase in temperature was moderate, we found that the equation of state became steeper (i.e. γ became higher). As the curvature statistics uses the whole spectra, it should be sensitive to changes in both T_0 and γ . Therefore, we now discuss how the detectability of the heating effect depends on the initial value of x_{HeII} . This, in turn, can be connected to early reionization of both H I and He II by massive stars in single-step models (Venkatesan, Tumlinson & Shull

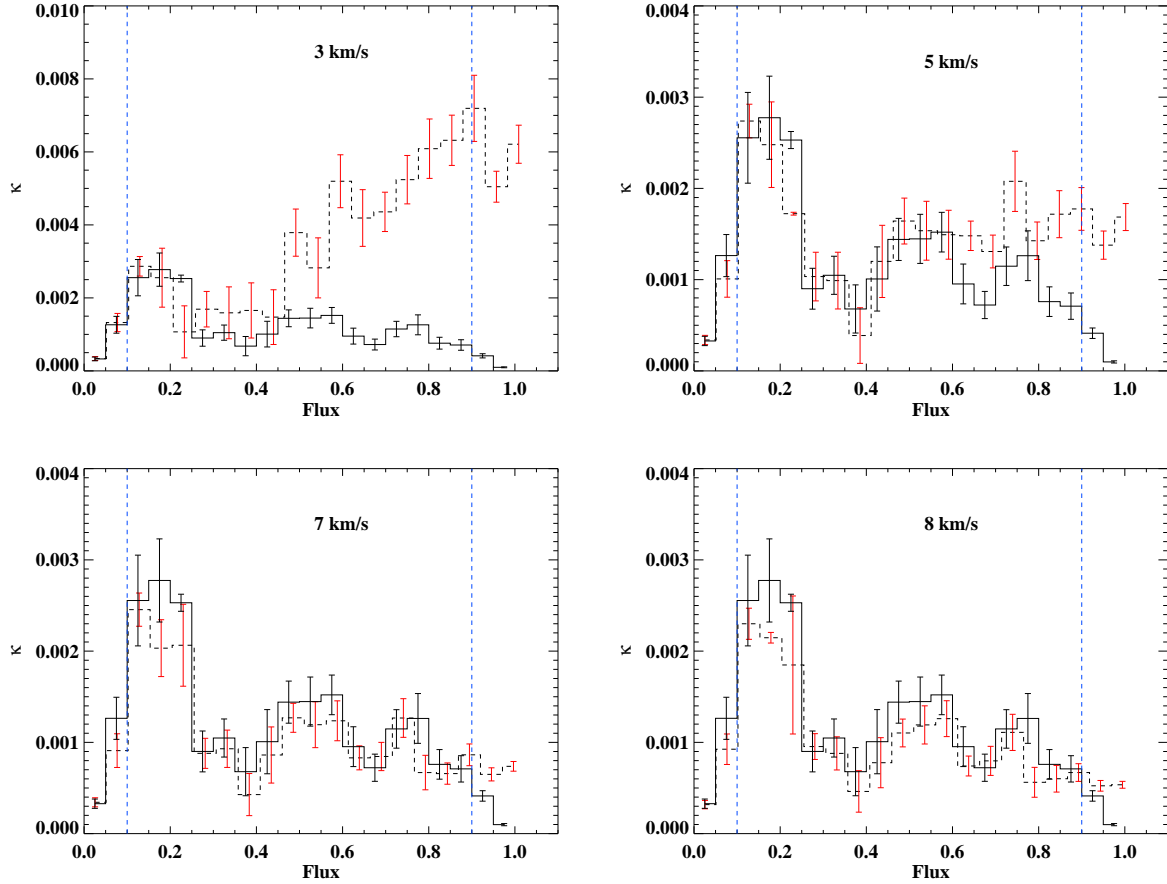


Figure 11. The average κ and the associated error in different flux bins are plotted versus flux (for the control spectrum). These plots show the approach of the convolved flux- κ distribution (dashed lines) to the non-noise added (ideal) distribution (solid lines) using different smoothing velocities, 3 km/s, 5 km/s, 7 km/s and 8 km/s from top left to bottom right. The blue dotted lines indicate the limits of the range in flux used for all the curvature statistics ($0.1 \leq \text{Flux} \leq 0.9$). It can be seen that the smoothing velocity of 7 km/s (bottom left) most closely resembles the ideal distribution.

2003; Wyithe & Loeb 2003; Choudhury & Ferrara 2005, 2006). In the single-step model of reionization, Population III stars reionize both H I and He II at redshifts $z > 6$. In some single-step models (Venkatesan, Tumlinson & Shull 2003), the fraction of helium in He III may hence reach about 60% by $z \sim 5.6$, which translates into x_{HeII} being only of the order of ~ 0.4 .

In order to investigate the effect of a lower initial x_{HeII} in the quasar near-zone, we consider different values of the metagalactic background $\Gamma_{\text{HeII}}^{\text{bg}}$ which translates into varying the initial He II fraction, x_{HeII} , and investigate the detectability of the additional heating to the variation of x_{HeII} . The fiducial equation of state parameters, $T_0 = 10^4$ K, and $\gamma = 1.3$ are used in this study. For each value of $\Gamma_{\text{HeII}}^{\text{bg}}$ which we consider, we generate “control” and “heated” spectra, then these two samples are compared using the 2d Kolmogorov-Smirnov statistic. The results are indicated in Table 3.

The table shows that the effect of the additional heating is more apparent if the initial fraction of x_{HeII} is greater. This is to be expected from the qualitative indications in Fig. 1, since a greater x_{HeII} fraction leads to a higher final (heated) temperature, and hence a greater difference between the control and the heated samples. The argument may be reversed to provide constraints on the metagalactic He II background required before the quasar is turned on, in order for the the additional heating effect to be de-

tected at a particular level. For example, with all other parameters being equivalent, if the additional heating effect is to be detected with greater than 75 % confidence, then the initial He II fraction in the vicinity of the quasar is constrained to $\gtrsim 0.74$, which, in turn, constrains the $\Gamma_{\text{HeII}}^{\text{bg}}$ to $\lesssim 10^{-17}$. Consequently, we infer that in single-step models of reionization where the x_{HeII} in the quasar vicinity takes very small values, the additional heating effect may be considerably less detectable than in two-step models, which allow for a greater He II fraction in the quasar near-zone.

Hence, we have effectively probed the sensitivity of the curvature statistic to the initial He II fraction in the vicinity of the quasar. However, as we saw in Sec. 3, the change in the He II fraction leads to both, a moderate increase in temperature as well as a steepening of the slope. In the preceding subsections while discussing the curvature statistics, we have kept the value of the $\Gamma_{\text{HeII}}^{\text{bg}}$ fixed at the HM12 value. This, as we have seen in Sec. 3, leads to a shift in the overall equation of state with no apparent change in slope. Hence, by performing the KS test in the previous subsections, we have equivalently captured the sensitivity of the curvature statistics to a change in the overall normalization, and seen that an overall normalization shift may be readily distinguished even with a sample of 512 pixels. Here, we briefly indicate the complementary effect, i.e. the sensitivity of the curvature statistic to a change in the slope

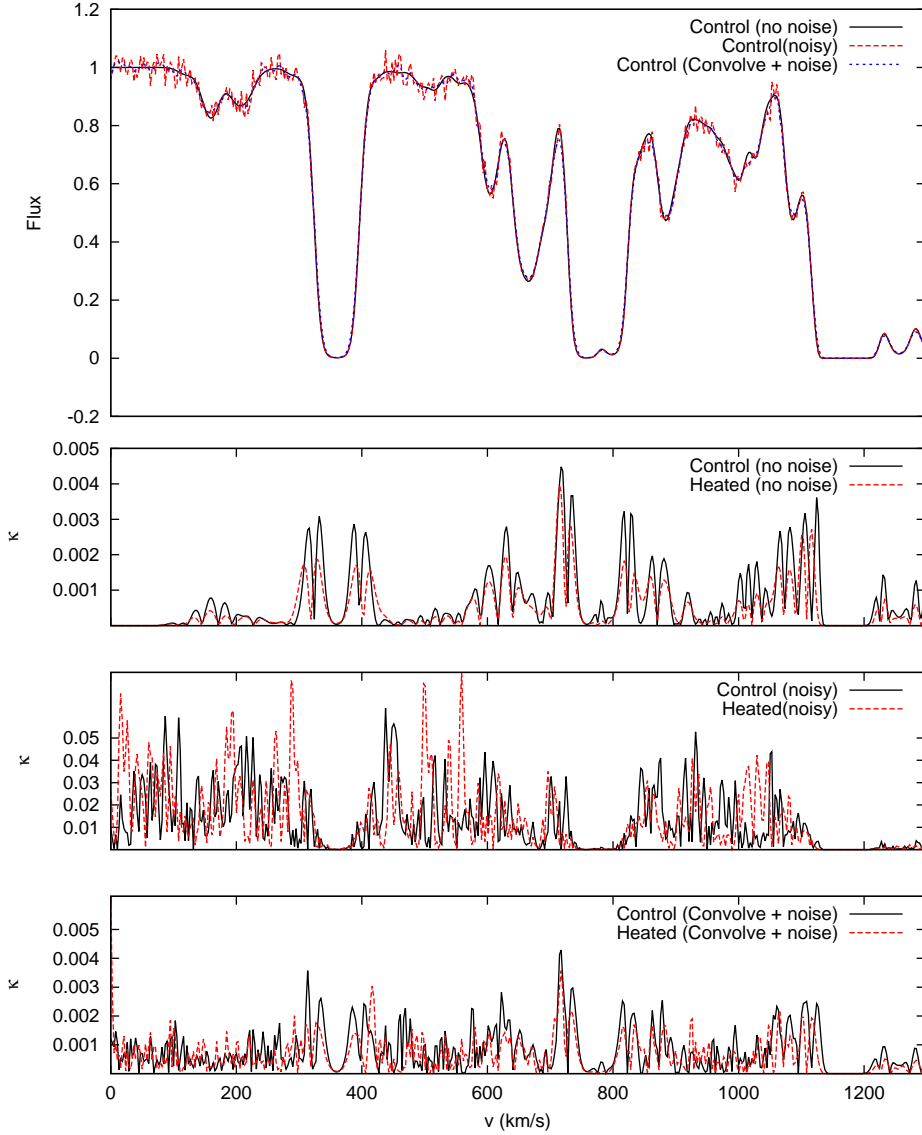


Figure 12. *Top panel:* The (control) quasar spectrum for the three cases : no noise added, noise added and noise convolved with the Gaussian filter of 7 km/s. It may be seen that the convolution with the Gaussian filter closely approximates the ideal distribution. *Lower three panels:* The curvature parameter as a function of pixel for three cases from top to bottom : no noise added, noise added, and noise convolved with the Gaussian filter of 7 km/s, for both the heated and the control samples along a line-of-sight.

alone. Note that this effect would not be captured in the previous tests with the curvature statistics, since the small (HM12) value of $\Gamma_{\text{HeII}}^{\text{bg}}$ considered therein, ensured that the slope change between the control and heated samples was negligible. We have seen in Fig. 3 in Sec. 3 that the maximum expected change in the initial $\gamma = 1.3$, for the lowest initial temperatures and He II fractions under consideration, is of the order of $\Delta\gamma = 0.1$. We find that a sample of 512 pixels can distinguish $\Delta\gamma = \pm 0.1$ with only about 7% - 39% confidence. If one also takes into account the observational and other sources of errors, we speculate that the allowed change (~ 0.1) in γ may be more difficult to detect statistically than the allowed change ($\sim 1000 - 5000$ K) in T_0 . This also shows us that the curvature statistic is more sensitive to the detection of the change

in the normalization than to the change in the slope of the equation of state.

4.4 Influence of other effects

Here, we provide discussions of the other factors that may also influence the observed spectra in the quasar near-zones, and an analysis on their significance for this study.

(i) Quasars in biased regions: In order to explore the effects of locating quasars in biased regions, we extracted spectra by placing the quasar at the most massive halo (mass $\sim 1.49 \times 10^{11} h^{-1} M_{\odot}$) in the simulation box. The baryonic overdensities around the quasar

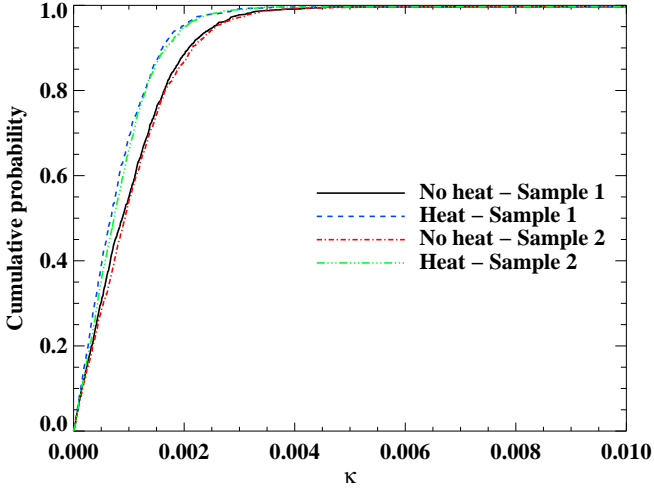


Figure 13. The cumulative probability distribution of the curvature statistic, κ , for two samples each of control and heated spectra. Each sample comprises 10 lines-of-sight (5120 pixels). The blue dashed and green dot-dot-dot-dashed curves represent the heated samples and the black solid and red dot-dashed curves represent the control ones. It can be seen that the effect of the additional heating is well above the cosmic variance of the individual samples. This figure may be compared with Fig. 9 where the opposite effect was noted.

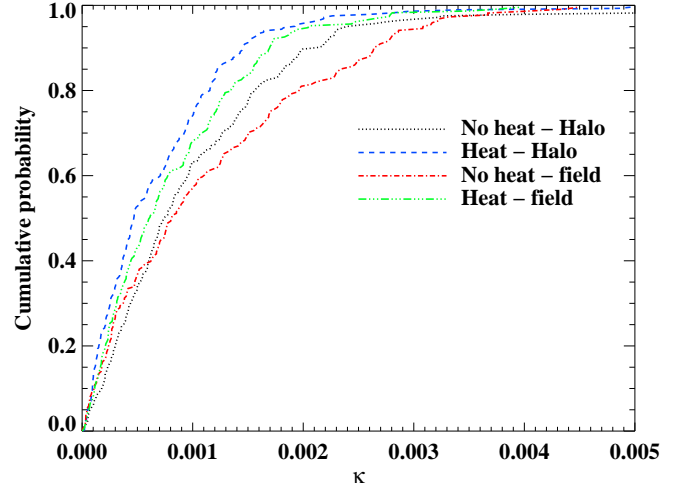


Figure 14. Cumulative probability distribution along a sightline, for the curvature for the halo and field locations of the quasars. The median values of curvature are lower in the case of quasars residing in biased locations, corresponding to higher temperatures both for the initial and heated spectra.

$\Gamma_{\text{HeII}}^{\text{bg}}$ (in units of HM12)	$x_{\text{HeII}}(\text{initial})$	2d KS prob
10^4	0.040	0.501
10^3	0.260	0.291
10^2	0.741	0.210
10	0.963	0.148
1	0.996	0.146

Table 3. This table indicates the two-dimensional KS test probabilities of the flux- κ joint distribution for different initial He II fractions with a sample of 512 pixels (1 line-of-sight). The KS test is performed between the control and the heated samples. It can be seen that the distinguishability of the samples decreases if the initial He II fraction is lower (or equivalently, if the He II metagalactic background is higher), thus quantifying the dependence of the additional heating effect on the initial He II fraction. In the above table, the initial equation of state is fixed at the fiducial value ($T_0 = 10000$ K, $\gamma = 1.3$.)

are found to be $\sim 10 - 50$, and hence, on applying the equation of state, the initial temperatures are $\sim 20000 - 35000$ K. The curvature median values for biased locations of the quasar are slightly lower than those for unbiased locations, as plotted in Fig. 14.

From the plots in Fig. 1, we speculate that there arises a degeneracy between the heating effects and the overdensities in the vicinity of the quasars when the quasars are modelled in biased locations. Temperatures of $T_0 \sim 20000$ K at redshift 6 arise in models where reionization occurs relatively late, $z_{\text{re}} \lesssim 8$. Therefore, the density enhancement and consequent temperature enhancement in biased locations may lead to estimates of a later epoch of reionization, than if the quasars are modelled in unbiased regions. A caveat to this discussion is the assumption of the initial equation of state being valid even at large overdensities of 10-50 that arise in biased regions. A detailed treatment including the effects of shocks, etc.

may be required to estimate the initial temperatures in these cases. However, this effect is expected to be minor, as indicated by the findings of Raskutti et al. (2012).

(ii) Three-dimensional effects and the environment: Our simulations use a 1D treatment of radiative transfer. In reality, the quasar radiates in 3D with some finite opening angle. However, since the observations of quasar spectra and the Lyman- α forest are always along a line-of-sight or a set of several sightlines, the line-of-sight treatment of radiative transfer is adequate for producing simulated spectra and for the further statistical analyses.

Recently, Morselli et al. (2014) have detected the presence of galaxy overdensities in the environment of four $z \sim 6$ quasars. As stellar spectra are generally soft, there is negligible emission above 4 Ryd from galaxies, which is required for the ionization of He II. In other words, while the value of Γ_{HI} may be changed slightly, there is negligible contribution to Γ_{HeII} from the galaxies. Since the dominant contribution to the heating effect comes from the ionization of He II, the heating effects and their detectability are influenced very little by the galaxies in the quasar environment.

(iii) Variations in background HI ionizing flux: We assume a uniform value of $\Gamma_{\text{HI}}^{\text{bg}}$ in the general IGM prior to the “switching on” of the quasar. Close to reionization, the value of $\Gamma_{\text{HI}}^{\text{bg}}$ may show spatial variations. However, our results do not change significantly since they are not sensitive to the actual value of $\Gamma_{\text{HI}}^{\text{bg}}$. Essentially, in the near-zone, the quasar ionizing flux dominates the background (by about a factor of 100 or more). Hence, small fluctuations in the initial $\Gamma_{\text{HI}}^{\text{bg}}$ are not expected to have a significant impact on the results and statistical analyses.

5 SUMMARY OF MAIN RESULTS

In this paper, we used detailed hydrodynamical simulations to provide an analysis of the features associated with the heating due to the ionization of He II in the near-zones of high-redshift quasars, and their implications for constraining the epochs of H I and He II reionization. Our main findings may be summarized as follows:

(i) We have seen that the measured temperature (Bolton et al. 2012) in the quasar near-zones arises from a combination of two effects : the initial He II fraction in the quasar vicinity, and the normalization of the initial equation of state of the IGM. If the initial temperature at mean density is $\lesssim 8000$ K, the measured temperature in the quasar near-zones is higher than that expected for the allowed range of initial He II fractions ($x_{\text{HeII}} = 0.04 - 1$) in the quasar vicinity. This shows that the temperature measurement can be used to place constraints on (a) the epoch and temperature of hydrogen reionization, and (b) single-step models of reionization that predict the initial He II fraction.

(ii) We recover the expected linear relationship of ΔT_0 increasing with the initial helium fraction x_{HeII} . Akin to the $\Delta T - x_{\text{HeII}}$ relation discussed in the literature (Furlanetto & Oh 2008), we also demonstrate a $\Delta\gamma - x_{\text{HeII}}$ relation, which shows a decrease in $\Delta\gamma$ with increasing x_{HeII} and a flattening out at the lowest x_{HeII} values, thus illustrating the steepening of the equation of state with decrease in the He II fraction in the quasar vicinity. Observationally, this steepening effect, which persists even for high initial temperatures where ΔT_0 is low, may also be used to constrain the near-zone He II fraction. However, the maximum expected increase in the slope may be more difficult to detect observationally than the expected shift in the overall normalization.

(iii) Optical depth effects are coupled to the propagation of the ionization front in the radiative transfer, so that we obtain a handle on the extent of the near-zone of He III, where the additional heating is expected to contribute significantly. If the quasar age is ~ 100 Myr, more than 80% of the H I proximity zone is heated in 78% of the sightlines. The heated fraction of the H I proximity zone is only about 30% - 35% for quasar lifetimes of ~ 10 Myr. This indicates that including the entire extent of the H I proximity zone for the temperature enhancement may result in some dilution of the statistics when the quasar lifetimes are short. However, considering the entire proximity zone of H I is a valid approximation if the quasar lifetimes are longer, $\gtrsim 100$ Myr. This is also the timescale for the saturation of the heating effect, making it fairly independent of distance.

(iv) We have quantified the effect of additional heating by using the flux PDF and curvature statistics to compare the real spectra to the simulated spectra without heating. We have noted that the sensitivity of the curvature statistic to the noise in the spectra may be effectively removed by smoothing with a Gaussian filter with a velocity width of 7 km/s. Both these statistics indicate that a higher value of T_0 and/or γ leads to less detectability of the effect of additional heating. This connects the additional heating due to He II reionization, to the epoch of hydrogen reionization.

(v) We find that the curvature statistic provides far more effective distinguishability of the heating effect, which is over and above the cosmic variance of individual samples of 10 lines-of-sight each having 512 pixels (chosen to match the typical sample sizes available in observations of seven quasars at redshift ~ 6). We also find that the detectability of the heating effect is dependent on the initial He II fraction in the quasar vicinity, with a greater He II fraction leading to greater detectability.

6 ACKNOWLEDGEMENTS

The research of HP is supported by the Shyama Prasad Mukherjee research grant of the Council of Scientific and Industrial Research (CSIR), India. The hydrodynamical simulations were performed using the Cetus and Perseus clusters of the IUCAA High Perfor-

mance Computing Centre. HP thanks Jayanti Prasad and Vikram Khaire for helpful discussions. We thank George Becker, James Bolton, Martin Haehnelt, T. Padmanabhan, Patrick Petitjean and David Syphers for useful comments on the manuscript. We thank the anonymous referee for helpful suggestions that improved the quality of the presentation.

REFERENCES

- Anninos P., Zhang Y., Abel T., Norman M. L., 1997, *New Astronomy*, 2, 209
 Assef R. J. et al., 2011, *ApJ*, 728, 56
 Bañados E., Venemans B., Walter F., Kurk J., Overzier R., Ouchi M., 2013, *ApJ*, 773, 178
 Becker G. D., Bolton J. S., Haehnelt M. G., Sargent W. L. W., 2011, *MNRAS*, 410, 1096
 Bolton J. S., Becker G. D., Raskutti S., Wyithe J. S. B., Haehnelt M. G., Sargent W. L. W., 2012, *MNRAS*, 419, 2880
 Bolton J. S., Becker G. D., Wyithe J. S. B., Haehnelt M. G., Sargent W. L. W., 2010, *MNRAS*, 406, 612
 Bolton J. S., Haehnelt M. G., 2007a, *MNRAS*, 374, 493
 Bolton J. S., Haehnelt M. G., 2007b, *MNRAS*, 382, 325
 Calverley A. P., Becker G. D., Haehnelt M. G., Bolton J. S., 2011, *MNRAS*, 412, 2543
 Cassata P. et al., 2013, *A&A*, 556, A68
 Choudhury T. R., Ferrara A., 2005, *MNRAS*, 361, 577
 Choudhury T. R., Ferrara A., 2006, *MNRAS*, 371, L55
 Choudhury T. R., Srianand R., Padmanabhan T., 2001, *ApJ*, 559, 29
 Ciardi B., Bolton J. S., Maselli A., Graziani L., 2012, *MNRAS*, 423, 558
 Eisenstein D. J., Hu W., 1999, *ApJ*, 511, 5
 Fan X., Carilli C. L., Keating B., 2006, *ARA&A*, 44, 415
 Fanidakis N., Macciò A. V., Baugh C. M., Lacey C. G., Frenk C. S., 2013, *MNRAS*, 436, 315
 Fardal M. A., Giroux M. L., Shull J. M., 1998, *AJ*, 115, 2206
 Faucher-Giguère C.-A., Lidz A., Hernquist L., Zaldarriaga M., 2008, *ApJ*, 688, 85
 Fukugita M., Kawasaki M., 1994, *MNRAS*, 269, 563
 Furlanetto S. R., 2009, *ApJ*, 703, 702
 Furlanetto S. R., Oh S. P., 2008, *ApJ*, 682, 14
 Furlanetto S. R., Oh S. P., Briggs F. H., 2006, *Phys. Repts.*, 433, 181
 Guimarães R., Petitjean P., Rollinde E., de Carvalho R. R., Djorgovski S. G., Srianand R., Aghaee A., Castro S., 2007, *MNRAS*, 377, 657
 Gunn J. E., Peterson B. A., 1965, *ApJ*, 142, 1633
 Haardt F., Madau P., 2012, *ApJ*, 746, 125
 Haiman Z., Cen R., 2002, *ApJ*, 578, 702
 Hui L., Gnedin N. Y., 1997, *MNRAS*, 292, 27
 Icke V., 1979, *ApJ*, 234, 615
 Inoue A. K. et al., 2011, *MNRAS*, 411, 2336
 Ishida E. E. O., de Souza R. S., Ferrara A., 2011, *MNRAS*, 418, 500
 Jakobsen P., Boksenberg A., Deharveng J. M., Greenfield P., Jędrzejewski R., Paresce F., 1994, *Nature*, 370, 35
 Jimenez R., Haiman Z., 2006, *Nature*, 440, 501
 Kashikawa N. et al., 2006, *ApJ*, 648, 7
 Khaire V., Srianand R., 2013, *MNRAS*, 431, L53
 Kim S. et al., 2009, *ApJ*, 695, 809

Kistler M. D., Yüksel H., Beacom J. F., Hopkins A. M., Wyithe J. S. B., 2009, *ApJ*, 705, L104
 Komatsu E. et al., 2011, *ApJS*, 192, 18
 Larson D. et al., 2011, *ApJS*, 192, 16
 Masters D. et al., 2012, *ApJ*, 755, 169
 McDonald P., Miralda-Escudé J., Rauch M., Sargent W. L. W., Barlow T. A., Cen R., 2001, *ApJ*, 562, 52
 McQuinn M., 2012, *MNRAS*, 426, 1349
 Mitra S., Choudhury T. R., Ferrara A., 2011, *MNRAS*, 413, 1569
 Mitra S., Choudhury T. R., Ferrara A., 2012, *MNRAS*, 419, 1480
 Mo H., van den Bosch F. C., White S., 2010, *Galaxy Formation and Evolution*
 Morselli L. et al., 2014, arXiv:1406.3961
 Mortlock D. J. et al., 2011, *Nature*, 474, 616
 Nakamura E., Inoue A. K., Hayashino T., Horie M., Kousai K., Fujii T., Matsuda Y., 2011, *MNRAS*, 412, 2579
 Oh S. P., Nollett K. M., Madau P., Wasserburg G. J., 2001, *ApJ*, 562, L1
 Olive K. A., Skillman E. D., 2004, *ApJ*, 617, 29
 Ouchi M. et al., 2010, *ApJ*, 723, 869
 Planck Collaboration et al., 2013, arXiv:1303.5076
 Press W. H., Teukolsky S. A., Vetterling W. T., Flannery B. P., 1992, *Numerical recipes in FORTRAN. The art of scientific computing*
 Pritchard J., Loeb A., 2010, *Nature*, 468, 772
 Pritchard J. R., Loeb A., Wyithe S., 2010, in *Bulletin of the American Astronomical Society*, Vol. 42, American Astronomical Society Meeting Abstracts 215, p. 460.12
 Raskutti S., Bolton J. S., Wyithe J. S. B., Becker G. D., 2012, *MNRAS*, 421, 1969
 Reimers D., Fechner C., Hagen H.-J., Jakobsen P., Tytler D., Kirkman D., 2005, *A&A*, 442, 63
 Ricotti M., Gnedin N. Y., Shull J. M., 2000, *ApJ*, 534, 41
 Robertson B. E., Ellis R. S., 2012, *ApJ*, 744, 95
 Rollinde E., Srianand R., Theuns T., Petitjean P., Chand H., 2005, *MNRAS*, 361, 1015
 Schaye J., Theuns T., Rauch M., Efstathiou G., Sargent W. L. W., 2000, *MNRAS*, 318, 817
 Seljak U., Slosar A., McDonald P., 2006, *JCAP*, 10, 14
 Shull J. M., France K., Danforth C. W., Smith B., Tumlinson J., 2010, *ApJ*, 722, 1312
 Springel V., 2005, *MNRAS*, 364, 1105
 Stark D. P., Ellis R. S., Richard J., Kneib J.-P., Smith G. P., Santos M. R., 2007, *ApJ*, 663, 10
 Syphers D., Shull J. M., 2014, *The Astrophysical Journal*, 784, 42
 Theuns T., Schaye J., Zaroubi S., Kim T.-S., Tzanavaris P., Carswell B., 2002, *ApJ*, 567, L103
 Theuns T., Zaroubi S., 2000, *MNRAS*, 317, 989
 Tornatore L., Ferrara A., Schneider R., 2007, *MNRAS*, 382, 945
 Totani T., Kawai N., Kosugi G., Aoki K., Yamada T., Iye M., Ohta K., Hattori T., 2006, *PASJ*, 58, 485
 Venkatesan A., Tumlinson J., Shull J. M., 2003, *ApJ*, 584, 621
 Viel M., Haehnelt M. G., Lewis A., 2006, *MNRAS*, 370, L51
 Walter F. et al., 2003, *Nature*, 424, 406
 Willott C. J. et al., 2007, *AJ*, 134, 2435
 Willott C. J., Percival W. J., McLure R. J., Crampton D., Hutchings J. B., Jarvis M. J., Sawicki M., Simard L., 2005, *ApJ*, 626, 657
 Worseck G. et al., 2011, *ApJ*, 733, L24
 Wyithe J. S. B., Bolton J. S., 2011, *MNRAS*, 412, 1926
 Wyithe J. S. B., Loeb A., 2003, *ApJ*, 586, 693
 Zheng W. et al., 2004, *ApJ*, 605, 631

APPENDIX A: CALCULATIONAL DETAILS

In this appendix, we present the details of the calculations which were described briefly in Section 2. The initial conditions are described by photoionization equilibrium with the background, this system of equations is given by:

$$\begin{aligned}
 n_{\text{HI}}\Gamma_{\text{HI}}^{\text{bg}} &= n_{\text{HII}}n_e\alpha_{\text{HII}} \\
 n_{\text{HeI}}\Gamma_{\text{HeI}}^{\text{bg}} + n_{\text{HeIII}}n_e\alpha_{\text{HeIII}} &= n_{\text{HeII}}\Gamma_{\text{HeII}}^{\text{bg}} + n_{\text{HeII}}n_e\alpha_{\text{HeII}} \\
 n_{\text{HeII}}\Gamma_{\text{HeII}}^{\text{bg}} &= n_{\text{HeIII}}n_e\alpha_{\text{HeIII}} \quad (\text{A1})
 \end{aligned}$$

with the boundary conditions that: $n_{\text{HI}} + n_{\text{HII}} = n_{\text{H}}$, $n_{\text{HeI}} + n_{\text{HeII}} + n_{\text{HeIII}} = n_{\text{He}}$, and $n_{\text{HII}} + n_{\text{HeII}} + 2n_{\text{HeIII}} = n_e$. Here, Γ_x^{bg} represents the photoionization rate of species ‘x’ from the background ionizing radiation assumed (we use Haardt & Madau 2012), the α ’s are the radiative recombination rate coefficients, and the n ’s represent the (proper) number densities.

The background photoionization rates are given by (in s^{-1}):

$$\begin{aligned}
 \Gamma_{\text{HI}}^{\text{bg}} &= 2.30 \times 10^{-13}; \quad \Gamma_{\text{HeI}}^{\text{bg}} = 1.54 \times 10^{-13}; \\
 \Gamma_{\text{HeII}}^{\text{bg}} &= 4.42 \times 10^{-19}. \quad (\text{A2})
 \end{aligned}$$

The temperatures are assigned to each pixel by the equation of state:

$$T(x, z) = T_0(z)[1 + \delta(x)]^{\gamma-1} \quad (\text{A3})$$

where, T_0 is the normalization temperature, $\delta(x)$ is the overdensity at the pixel and γ is the slope of the equation of state.

Our numerical procedure now involves solving the system of four differential equations for the temperature evolution and hydrogen and helium ion densities evolution:

$$\begin{aligned}
 \frac{dn_{\text{HII}}}{dt} &= n_{\text{HI}}\Gamma_{\text{HI}} - n_{\text{HII}}n_e\alpha_{\text{HII}} - 3H(t)n_{\text{HII}} \\
 \frac{dn_{\text{HeII}}}{dt} &= n_{\text{HeI}}\Gamma_{\text{HeI}} + n_{\text{HeIII}}n_e\alpha_{\text{HeIII}} \\
 &\quad - n_{\text{HeII}}\Gamma_{\text{HeII}} - n_{\text{HeII}}n_e\alpha_{\text{HeII}} - 3H(t)n_{\text{HeII}} \\
 \frac{dn_{\text{HeIII}}}{dt} &= n_{\text{HeII}}\Gamma_{\text{HeII}} - n_{\text{HeIII}}n_e\alpha_{\text{HeIII}} - 3H(t)n_{\text{HeIII}} \\
 \frac{dT}{dt} &= \frac{2}{3k_B n_{\text{tot}}} [H_{\text{tot}}(n_i) - C(n_i, T)] \\
 &\quad - 2H(t)T - \frac{T}{n_{\text{tot}}} \frac{dn_{\text{tot}}}{dt} \quad (\text{A4})
 \end{aligned}$$

In the above equations, Γ_x represents the photoionization rates of species ‘x’ (contributed both by the quasar as well as the background in the near-zone, and by the background alone, for the far zone). The adiabatic index is $5/3$, and $H_{\text{tot}}(n_i)$ and $C(n_i, T)$ represent the total photoheating rate per unit volume, and radiative cooling function respectively. The Hubble parameter is $H(t)$, and $n_{\text{tot}} = n_{\text{H}} + n_{\text{He}} + n_e$ is the total number density of particles of different species. The term $-2H(t)T$ in the temperature evolution equation represents the contribution of the expansion of the universe to the adiabatic cooling of the gas. We ignore the contribution from $-3H(t)n$ in the evolution of the species densities, since the ionization time scales under consideration are much smaller than $H^{-1}(t)$. The last term $-T(dn_{\text{tot}}/dt)/n_{\text{tot}}$ represents the correction due to species evolution. This correction is only about 1 part in 10^3 at the highest temperatures, but the effect is expected to be important in the initial stages of evolution.

The photoionization rates from the quasar at a distance R are given by:

$$\begin{aligned}
 \Gamma_{\text{HI}}^{QSO}(R) &= \int_{\nu_{\text{HI}}}^{\infty} \frac{L_{\nu}}{4\pi R^2 h\nu} \sigma_{\text{HI}}(\nu) \exp(-\tau_{\text{HI}}) d\nu; \\
 \Gamma_{\text{HeI}}^{QSO}(R) &= \int_{\nu_{\text{HeI}}}^{\infty} \frac{L_{\nu}}{4\pi R^2 h\nu} \sigma_{\text{HeI}}(\nu) \exp(-\tau_{\text{HeI}}) d\nu \\
 \Gamma_{\text{HeII}}^{QSO}(R) &= \int_{\nu_{\text{HeII}}}^{\infty} \frac{L_{\nu}}{4\pi R^2 h\nu} \sigma_{\text{HeII}}(\nu) \exp(-\tau_{\text{HeII}}) d\nu \quad (\text{A5})
 \end{aligned}$$

where $L_{\nu} = L_{\text{HI}}(\nu/\nu_{\text{HI}})^{-\alpha_s}$. The $\sigma(\nu)$'s denote the photoionization cross-sections for H I, He I and He II respectively and the τ 's are the corresponding optical depths, calculated as

$$\begin{aligned}
 \tau_x(R) &= \sum_{i=1}^{n(R)} [n_{\text{HI}}(i)\sigma_{\text{HI}}(\nu_x) + n_{\text{HeI}}(i)\sigma_{\text{HeI}}(\nu_x) \\
 &+ n_{\text{HeII}}(i)\sigma_{\text{HeII}}(\nu_x)]l \quad (\text{A6})
 \end{aligned}$$

where, l is the pixel size and ν_x is the ionization edge of species $x = \text{H I}, \text{He I}$ or He II . For simplicity of computation, we only consider the optical depth at the ionization edge of the relevant species in the photoionization rate. The sum is over all the pixels up to the $n(R)$ th pixel which is at the distance R from the quasar. The total photoionization rate is obtained by adding the contributions from the quasar [Eq. (A5)] and the metagalactic background [Eq. (A2)].

Recombination rates are as given in Fukugita & Kawasaki (1994), Anninos et al. (1997) and Mo, van den Bosch & White (2010) for H II, He II (including dielectronic recombination) and He III. We use case A recombination coefficients here as they have been found to be the appropriate choice for comparison with hydrodynamical simulations of quasar near-zones (Bolton & Haehnelt 2007a). The details are as follows:

- (i) Case A recombination coefficients (in cm^3s^{-1}):
 - (a) $\alpha_{\text{HII}} = 6.28 \times 10^{-11} T^{-0.5} (T/1000)^{-0.2} (1 + (10^{-6}T)^{0.7})^{-1}$
 - (b) $\alpha_{\text{HeII}} = 1.5 \times 10^{-10} T^{-0.6353}$
 - (c) $\alpha_{\text{HeIII}} = 3.3 \times 10^{-10} T^{-0.5} (T/1000)^{-0.2} (1 + (2.5 \times 10^{-7}T)^{0.7})^{-1}$
- (ii) Dielectronic recombination coefficient for helium (in cm^3s^{-1}):
 - (a) $\alpha_{\text{HeII}}^d = 1.93 \times 10^{-3} T^{-1.5} \exp(-470000/T) (1 + 0.3 \exp(-94000/T))$

To analyze the photo-heating, we use the background heating rates as given in Haardt & Madau (2012) at redshift ~ 6 (in ergs s^{-1}):

$$\begin{aligned}
 E_{\text{HI}}^{\text{bg}} &= 1.5824 \times 10^{-24}; \quad E_{\text{HeI}}^{\text{bg}} = 1.792 \times 10^{-24}; \\
 E_{\text{HeII}}^{\text{bg}} &= 4.304 \times 10^{-29}. \quad (\text{A7})
 \end{aligned}$$

We add to the above background heating rates, the additional heating rate due to the quasar with the previously mentioned luminosity and spectral index, given by:

$$\begin{aligned}
 E_{\text{HI}}^{QSO}(R) &= \int_{\nu_{\text{HI}}}^{\infty} \frac{L_{\nu} h(\nu - \nu_{\text{HI}})}{4\pi R^2 h\nu} \sigma_{\text{HI}}(\nu) \exp(-\tau_{\text{HI}}) d\nu; \\
 E_{\text{HeI}}^{QSO}(R) &= \int_{\nu_{\text{HeI}}}^{\infty} \frac{L_{\nu} h(\nu - \nu_{\text{HeI}})}{4\pi R^2 h\nu} \sigma_{\text{HeI}}(\nu) \exp(-\tau_{\text{HeI}}) d\nu \\
 E_{\text{HeII}}^{QSO}(R) &= \int_{\nu_{\text{HeII}}}^{\infty} \frac{L_{\nu} h(\nu - \nu_{\text{HeII}})}{4\pi R^2 h\nu} \sigma_{\text{HeII}}(\nu) \exp(-\tau_{\text{HeII}}) d\nu \quad (\text{A8})
 \end{aligned}$$

At any distance R from the quasar, the total photoheating rate

per unit volume, $H_{\text{tot}}(R)$, is given by $H_{\text{tot}}(R) = \sum_i n_i [E_i^{\text{bg}} + E_i^{QSO}(R)]$ where the sum is over $i = \text{H I}, \text{He I}$ and He II .

The cooling function consists of contributions from (a) bremsstrahlung and (b) recombination. We use the corresponding expressions as given by Fukugita & Kawasaki (1994), Anninos et al. (1997) and Mo, van den Bosch & White (2010) for H II, He II and He III, including a contribution from the dielectronic recombination of He II. Collisional ionization and its associated cooling are ignored since, for the range of temperatures and densities considered here, their magnitudes are negligible as compared to the photoionization and the cooling rates by recombination and bremsstrahlung respectively, which we have considered here. The details are:

- (i) Recombination cooling rates (in $\text{erg cm}^{-3}\text{s}^{-1}$):
 - (a) $\Lambda_{\text{HII}} = 2.82 \times 10^{-26} T^{0.3} (1 + 3.54 \times 10^{-6} T)^{-1} n_{\text{HII}} n_e$
 - (b) $\Lambda_{\text{HeII}} = 1.55 \times 10^{-26} T^{0.3647} n_{\text{HeII}} n_e$
 - (c) $\Lambda_{\text{HeIII}} = 1.49 \times 10^{-25} T^{0.3} (1 + 0.885 \times 10^{-6} T)^{-1} n_{\text{HeIII}} n_e$
- (ii) Dielectronic recombination cooling rate for helium (in $\text{erg cm}^{-3}\text{s}^{-1}$):
 - (a) $\Lambda_{\text{HeII}}^d = 1.24 \times 10^{-13} T^{-1.5} \exp(-470000/T) (1 + 0.3 \exp(-94000/T)) n_{\text{HeII}} n_e$
 - (iii) Bremsstrahlung (in $\text{erg cm}^{-3}\text{s}^{-1}$):
 - $\Lambda_b = 1.43 \times 10^{-27} T^{0.5} g_{\text{ff}} n_e (n_{\text{HII}} + n_{\text{HeII}} + 4n_{\text{HeIII}})$ where, the Gaunt factor g_{ff} is given by $g_{\text{ff}} = 1.1 + 0.34 \exp(-5.5 - \log_{10} T)^2 / 3$.

A1 Description of the code

The algorithmic procedure is as outlined in Fig. A1. First, a number N lines of sight are extracted randomly in our simulation box at redshift 6. For each line of sight, the density and velocity fields, δ_b , and v_b of the baryonic particles are obtained. The equilibrium ion number densities and temperature are found under the assumption of photoionization with the metagalactic background and equation of state, by solving Eq. (A1) using the Newton-Raphson technique with the routine NEWT in Numerical Recipes (Press et al. 1992). The inputs to the code at this stage are T_0 , γ and the background photoionization rates.

Next, the line-of-sight is gridded into n equispaced intervals with the length of each interval being equal to the average pixel size in the simulation, and the quasar is placed at the first gridpoint. The inputs are the luminosity of the quasar at the Lyman-edge, L_{HI} , the spectral index α_s and the quasar lifetime t_Q . The start time of evolution of the thermal and ionization state of a gridpoint interval is decided by the time at which the He II ionization front reaches that gridpoint, which is calculated from Eq. (1) using the known distance to the gridpoint¹². The initial conditions are the equilibrium species fractions and temperatures found previously. The four rate equations in Eq. (A4) are now solved using a FORTRAN90 code based on the ODEINT routine of the Numerical Recipes (Press et al. 1992). The ion densities and temperatures at each gridpoint interval are evolved with a time-step Δt , which is dynamic in nature, being inversely proportional to the rate of ionizing photons at the distance of the gridpoint; a typical value being $\Delta t \sim 10^6$ s. We follow the approach of Bolton & Haehnelt (2007a) in that when the relative change in the electron number density falls

¹² Strictly speaking, one should evolve the gridpoint even if the He II front has not reached it, to account for the Hubble expansion. However, we do not do this since the time scales under present consideration are much shorter than $H^{-1}(t)$.

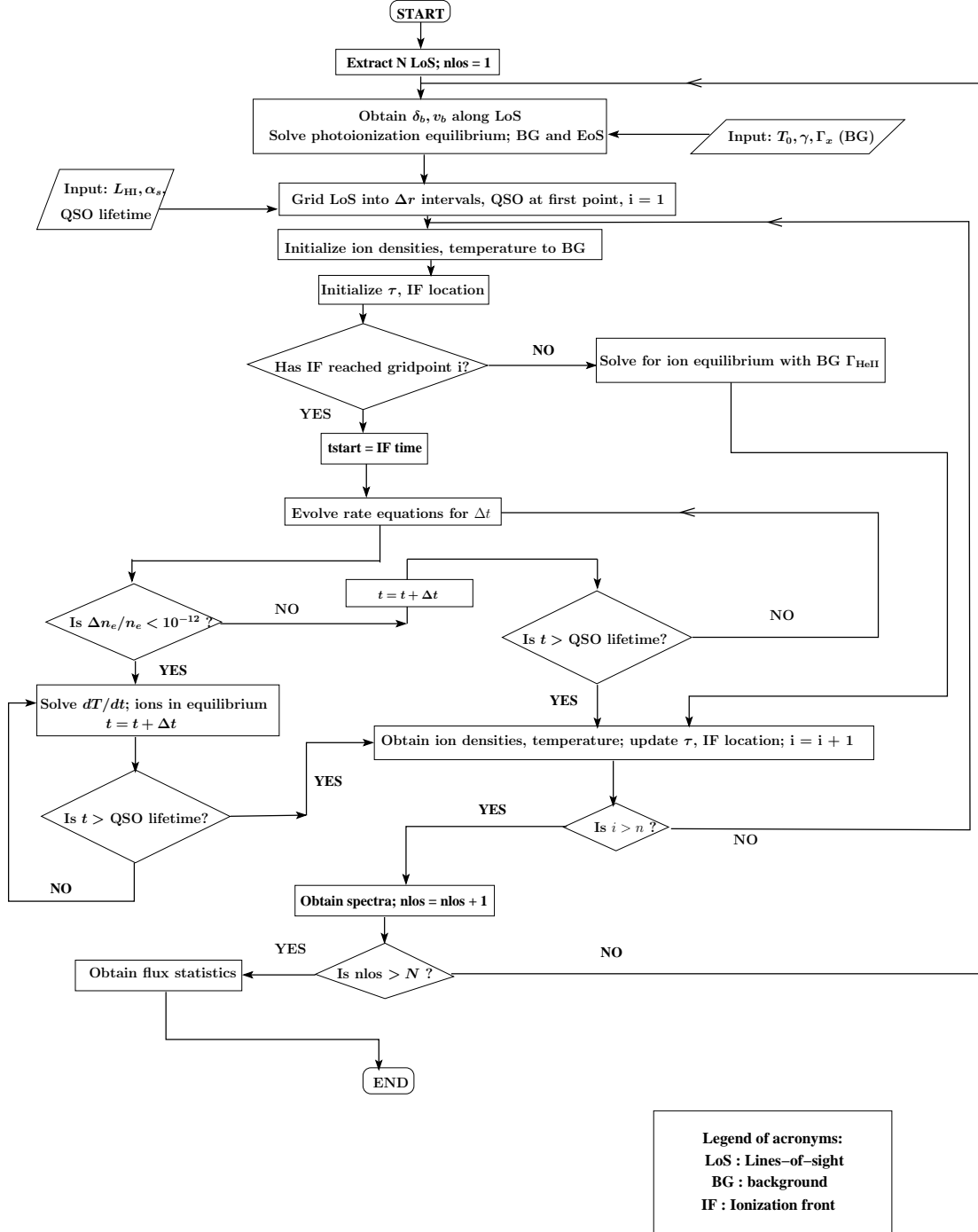


Figure A1. Flowchart describing the numerical scheme.

below 10^{-12} , the ion fractions are solved for assuming photoionization equilibrium and a larger time-step is considered.

In case the He II ionization front has not yet reached a particular gridpoint within the quasar lifetime, the temperatures and ion densities are solved for assuming photoionization equilibrium with no contribution from the quasar to Γ_{HeII} and E_{HeII} . Hence, those gridpoints located beyond the He II front do not “see” the quasar as far as photoionization of He II and the resulting gas heating are concerned. In this way, the location of the He II ionization front at the end of the quasar lifetime is also known.

The final values of number densities of different species and the temperature, for each gridpoint, are then used to update the optical depth values at the ionization edges, and the location of the He II ionization front. Once these values are passed to the next gridpoint, the process is repeated until the end of the line-of-sight is reached. The temperature and neutral hydrogen density at each pixel are used to generate the simulated spectrum along that line-of-sight, by defining the redshift grid as described in the previous section. Note that in this procedure, the optical depth value contributes to the determination of the location of the ionization front, which determines the start time of the next gridpoint and its consequent evolution, which in turn contributes to the optical depth for the further gridpoints under consideration. Hence, if the (integrated) optical depth effect becomes large enough so that the front is “stopped”, the subsequent gridpoints do not “see” the ionization and heating photons from the quasar, and are ionized and heated by the background alone.

Finally, the combined set of all the gridpoints at each line of sight, and the number of lines of sight extracted in the simulation box are used to obtain the flux statistics. In our simulations, we do not use the realistic quasar continuum to generate spectra. Hence, all the artificial effects coming from the issues related to continuum fitting will not be present in our analysis.